

1 **A method to control the environmental wind profile in idealized simulations**  
2 **of deep convection with surface friction**

3 Daniel T. Dawson II\*

4 *Department of Earth, Atmospheric, and Planetary Sciences, Purdue University, West Lafayette,*  
5 *Indiana*

6 Brett Roberts and Ming Xue

7 *Center for Analysis and Prediction of Storms and School of Meteorology, University of*  
8 *Oklahoma, Norman, Oklahoma*

9 *\*Corresponding author address: Daniel T. Dawson II, Department of Earth, Atmospheric, and*  
10 *Planetary Sciences, Purdue University, 550 Stadium Mall Dr., West Lafayette, IN 47906.*

11 E-mail: dandawson@purdue.edu

## ABSTRACT

12 In idealized, horizontally homogeneous, cloud model simulations of con-  
13 vective storms, the action of surface friction tends to modify the near-ground  
14 environmental wind profile over time, owing to the lack of a large-scale pres-  
15 sure gradient force to balance the frictional force together with the Coriolis  
16 force. This situation is undesirable for many applications where the impact of  
17 the low-level wind shear on the simulated storm behavior is the focus of inves-  
18 tigation, as it introduces additional variability in the experiment and accord-  
19 ingly complicates interpretation of the results. Partly for this reason, many  
20 researchers have opted to perform simulations with free-slip lower boundary  
21 conditions, which with appropriate boundary conditions allows for more pre-  
22 cise control of the large-scale environmental wind profile. Yet, some recent  
23 studies have advocated important roles of surface friction in storm dynamics.  
24 Here, a simple force-balance method for controlling or maintaining any cho-  
25 sen environmental wind profile or sounding in idealized storm simulations in  
26 the presence of surface friction and both resolved and subgrid-scale turbulent  
27 mixing is introduced. The method is demonstrated through comparisons of  
28 simulations of a tornadic supercell with and without surface friction and with  
29 or without invoking the new method. The method is compared with similar  
30 techniques in the literature and potential extensions and other applications are  
31 discussed.

## 32 **1. Introduction**

33 Idealized numerical modeling studies of convective storms have yielded many valuable insights  
34 into their behavior over the past few decades. The idealized modeling approach typically initial-  
35 izes a horizontally homogeneous "storm environment" that is defined by a single vertical profile  
36 (usually taken from a real-world sounding, extracted from NWP model output, or from analytical  
37 functions). This environment is assumed to be representative of large-scale (i.e. meso-alpha to  
38 synoptic) conditions and is usually but not always also assumed to be invariant in time (so that  
39 storm behavior within a given fixed environment can be studied). Convective development is then  
40 encouraged through a variety of artificial forcing mechanisms such as thermal bubbles (Klemp  
41 and Wilhelmson 1978), imposed low-level convergence (Loftus et al. 2008), and updraft nudging  
42 (Naylor and Gilmore 2012). These simplifications are reasonable if the simulation domain is on  
43 the order of 100 km in width and the simulation length is on the order of a few hours. They al-  
44 low for precise control over the background environment, and thus better understanding of how  
45 different environments (in particular the vertical structure of the environment) modulate the sim-  
46 ulated storm characteristics. Most studies of this type represent any forces operating on these  
47 large scales either by neglecting them entirely or by proscribing some initial balance condition:  
48 typically geostrophic balance.

49 If we examine the horizontal momentum equations as applied to the *horizontally homogeneous*  
50 *large-scale environment* (hereafter simply "environment") of an idealized storm simulation, it is  
51 clear that the horizontal pressure gradient force (PGF) terms are identically zero, since by defini-  
52 tion they depend on (large-scale) horizontal gradients in pressure. Therefore, in order to enforce  
53 geostrophic balance on the large scale while still maintaining horizontal homogeneity, the large-  
54 scale PGF must somehow be specified and *decoupled* from the actual model pressure field. We can

55 then write the horizontal momentum equations for the evolution of this large scale environment  
 56 as:

$$\begin{aligned}\frac{\partial U}{\partial t} &= PPGF_x + fV + F_x[U, V] \\ \frac{\partial V}{\partial t} &= PPGF_y - fU + F_y[U, V]\end{aligned}\tag{1}$$

57 where  $U$  and  $V$  are the horizontal wind components of the *horizontally homogeneous large-scale*  
 58 *environment* (i.e. sans storm-induced perturbations), and  $PPGF_x$  and  $PPGF_y$  are the horizontal  
 59 components of the *proscribed* large-scale "Pseudo-PGF" (hereafter just PPGF). We use the term  
 60 "Pseudo-PGF" in this paper because it does not correspond to any actual large-scale horizontal  
 61 pressure gradient in the model.  $F_x[U, V]$  and  $F_y[U, V]$  are the horizontal components of the fric-  
 62 tional force. These contain the parameterized sub-grid-scale turbulence mixing, computational  
 63 mixing/diffusion (and potentially imposed artificial mixing), and the surface drag that defines the  
 64 vertical momentum flux at the surface. The wind components are shown in brackets in these terms  
 65 to emphasize their use in the turbulent mixing and surface drag formulations.

66 Neglecting the friction terms for the moment, the enforcement of large scale geostrophic balance  
 67 then boils down to how to specify the PPGF components such that the RHS of (1) is zero at all  
 68 times and everywhere in the simulation domain. Under the assumption of geostrophic balance, the  
 69 PPGF is simply obtained from:

$$\begin{aligned}PPGF_x &= -fV_g \\ PPGF_y &= fU_g\end{aligned}\tag{2}$$

70 where  $U_g$  and  $V_g$  are the geostrophic wind components, usually assumed to be constant in time.  
 71 The environmental horizontal momentum equations then become:

$$\begin{aligned}\frac{\partial U}{\partial t} &= f(V - V_g) \\ \frac{\partial V}{\partial t} &= -f(U - U_g)\end{aligned}\tag{3}$$

72 Thus, the PPGF is specified in this case by the constraint of geostrophic balance and therefore  
73 does not appear *explicitly* in the momentum equations. A standard method in most idealized cloud  
74 models is to define the model *base state* using the geostrophic initial environment as defined here.  
75 Then,  $(U, V) = (U_g, V_g)$  and from (3) the environmental horizontal winds remain steady in time,  
76 as desired. Otherwise, it is easy to see from (3) that this is mathematically equivalent to applying  
77 the Coriolis force only to the *perturbation* winds relative to this initial environment. Generalizing  
78 (3) to include horizontally varying perturbation winds, this is a standard run-time option for most  
79 models when run in "idealized cloud model mode".

80 In addition to the PPGF and the Coriolis force, friction is another force that is active at large  
81 scales. It is most important in the boundary layer, and particularly near the surface where the mo-  
82 mentum flux from the surface dominates. In theory, when observed soundings are used to define  
83 the environment in idealized storm simulations, they should already be subject to the effects of  
84 friction. Under the aforementioned assumption of geostrophic balance (or no large scale forces  
85 at all), however, the introduction of surface friction tends to modify the specified environmental  
86 sounding during the simulation (especially in the low levels), by reducing the near surface wind  
87 speed (Adlerman and Droegemeier 2002; Wicker and Wilhelmson 1993). That is, the RHS of  
88 (3) now contains nonzero friction terms and the large-scale balance is upset. This problem has  
89 historically made it difficult to control the environmental wind profile while simultaneously incor-  
90 porating the effects of surface friction through, e.g., a drag parameterization or other imposition  
91 of no-slip or semi-slip lower boundary conditions. At least partly for this reason, the vast major-  
92 ity of idealized modeling studies have elected to use free-slip lower boundary conditions, thereby  
93 ignoring the effects of surface friction entirely.

94 However, it has long been recognized that the effects of surface friction are important for some  
95 aspects of severe convective storm behavior; a prime example is its role in tornado dynamics.

96 Surface friction plays an important role in tornado structure and evolution through the formation  
97 of intense radial inflow in a shallow surface layer and subsequent rapid upward turning in the  
98 corner flow region (e.g., Lewellen and Lewellen 2007; Fiedler and Rotunno 1986; Davies-Jones  
99 2014). Recent studies (Schenkman et al. 2014; Roberts et al. 2016; Markowski 2016; Mashiko  
100 2016; Roberts and Xue 2017) have additionally found that surface friction may be implicated in  
101 processes leading to supercell tornadogenesis including as a potential direct source of horizontal  
102 vorticity that can be tilted into the vertical within the developing tornado. These reasons, among  
103 others, have motivated researchers to develop methods to mitigate the deleterious effect of surface  
104 friction on the environmental wind profile while still incorporating its effects in simulations that  
105 include the tornado and its parent storm within the context of an idealized environment of the type  
106 discussed above.

107 Previous efforts to incorporate surface friction into idealized storm simulations have varied in  
108 their approach. Wicker and Wilhelmson (1993) were among the first to study the effects of surface  
109 friction on the development of a simulated tornado within the context of a full 3D supercell simu-  
110 lation. In their doubly-nested grid approach, they applied surface friction to a restart of their inner  
111 (120-m grid spacing) tornado-resolving grid, 900 s before tornadogenesis in the original, free-  
112 slip inner domain simulation. The outer grid (600-m grid spacing) maintained a free-slip lower  
113 boundary condition throughout the simulation period. In this manner, they were able to show that  
114 their simulated tornado responded to the presence of surface friction by contracting in radius and  
115 intensifying. In their case, the nested simulation after the introduction of friction was likely too  
116 short for significant changes to occur in the environmental wind profile, which was additionally  
117 maintained by the lateral boundary conditions from the no-friction outer grid.

118 Other studies have attempted to remove or mitigate the modification of the environmental wind  
119 profile due to the action of surface friction through various approaches. Wilhelmson and Chen

120 (1982, hereafter WC82) modified the surface drag formulation such that it was only applied to the  
121 perturbation wind (relative to the initial environmental wind profile). Adlerman and Droegemeier  
122 (2002) used the WC82 method in their idealized supercell simulations to study the effects of  
123 surface drag with different specified magnitudes of the drag coefficient on the behavior of the  
124 simulated mesocyclones. More recently, Roberts et al. (2016, hereafter R16) and Markowski  
125 (2016, hereafter M16) independently developed different methods by which surface drag could be  
126 incorporated into an idealized simulation framework while simultaneously maintaining a more-  
127 or-less unchanged environmental wind profile throughout a simulation. Coffey and Parker (2017)  
128 applied the R16 method to their idealized simulations of supercells in nontornadic and tornadic  
129 environments derived from composites of VORTEX-2 proximity soundings (Parker 2014).

130 The WC82, R16, and M16 methods can be cast within the context of a more general framework  
131 where friction is included in an (up to) three-way balance with the Coriolis and the PPGF. John-  
132 son Jr (1966) proposed the term *geotriptic* for this three-force balance (where, in addition to the  
133 surface friction itself, the internal turbulent eddy flux is also balanced). The rest of this paper is  
134 organized as follows: in section 2, we discuss these previous methods, introduce a new method  
135 that overcomes some of their limitations, and describe its implementation into a numerical cloud  
136 model. In Section 3, we test the new method with simulations of a supercell in an environment  
137 derived from the 24 May 2011 Oklahoma tornado outbreak. The simulations compare traditional  
138 free-slip simulations with the new method, with the WC82 base state surface drag removal method,  
139 and with unbalanced surface drag. Section 3 also describes the results of corresponding simula-  
140 tions in which the pre-storm environment includes resolved turbulent eddies. Section 4 describes  
141 and compares the structure and behavior of the simulated storm across the simulations, focusing  
142 on the structure of surface boundaries. Finally, section 5 summarizes the paper and discusses some  
143 potential modifications to the method and broader applications.

## 144 2. Description of the new method

### 145 a. Description of previous methods

146 As previously stated, including the effects of surface friction will necessarily cause a devia-  
147 tion from the typically assumed initial geostrophic balance in idealized storm simulations. R16  
148 addressed this problem by first running a 1D column simulation (representing the horizontally  
149 homogeneous environment) with the same vertical grid spacing, surface drag coefficient, and tur-  
150 bulence parameterization as in their fully 3D runs. They enforced an initial *geostrophic balance*.  
151 Thus, in their 1D simulation the only forces acting on the wind components were the PPGF (spec-  
152 ified via the assumption of initial geostrophic balance), the Coriolis force and friction:

$$\begin{aligned}\frac{\partial U}{\partial t} &= f(V - V_g) + F_x[U, V] \\ \frac{\partial V}{\partial t} &= -f(U - U_g) + F_y[U, V]\end{aligned}\tag{4}$$

153 During the column simulation these three forces together slowly modified the wind profile, even-  
154 tually reaching a steady state in approximate *geotriptic balance*. R16 then used this final balanced  
155 wind profile to initialize the environment of their 3D simulations; as such, the wind profile would  
156 remain in a quasi-steady state away from storm-induced perturbations.

157 Similar to R16, though not running a completely separate simulation, M16 sought a balanced  
158 wind profile by first allowing friction to modify the wind profile in their "toy model" supercell  
159 tornado simulations prior to the activation of the artificial heat source to initiate convection. Then  
160 after the first hour of this "adjustment" period, they applied a nudging term to the model horizontal  
161 momentum equations that slowly relaxed the horizontal mean wind profile back toward the mean  
162 profile as it was at 1 h simulation time. The wind profile reached a near-steady state by 2 h,  
163 at which point they activated their heat source to generate the "toy" supercell. Moreover, they  
164 excluded the Coriolis force from their simulations entirely; the nudging terms thus "crudely mimic

165 the influence of a large-scale horizontal pressure-gradient force and Coriolis force” (M16). The  
166 relaxation coefficient was chosen to minimize the impact on the storm-induced perturbations while  
167 still maintaining a constant ”far-field” environmental wind profile.

168 Finally, instead of assuming an initial *geostrophic* balance as in R16, WC82 assumed that the  
169 surface drag was *already* in balance with an assumed PPGF (and possibly also Coriolis force, if it  
170 is active in the simulation). In a manner reminiscent of modifying the Coriolis force in (3) via the  
171 geostrophic balance relations (2), WC82 modified the surface drag formulation so that the drag  
172 was only applied to the perturbation wind relative to the initial environmental wind profile.

### 173 *b. Description of the new method*

174 The WC82, M16, and R16 methods can each be viewed ultimately as methods to compute or  
175 specify a PPGF that is consistent with a large-scale three-way balance between the PPGF, Coriolis,  
176 and friction forces. Inspired by these previous efforts and in an attempt to overcome some of their  
177 limitations, we propose a new method to enforce this three-way balance (hereafter the ”Geotriptic  
178 Wind Balance”, or GWB method). The PPGF can be specified through the geotriptic wind balance  
179 relation:

$$PPGF_x = -fV - F_x[U, V] \tag{5}$$

$$PPGF_y = fU - F_y[U, V]$$

180 One may compute the needed PPGF, then, with knowledge of the large scale Coriolis and frictional  
181 forces in the model. Our method for doing so has a similar starting point to R16 and M16 in that  
182 we leverage the model integration sans any storm-induced perturbations. Specifically, we use the  
183 model state prior to the introduction of artificial forcing at or near the beginning of the simulation.  
184 Instead of enforcing geostrophic balance and running out to a steady state as in R16, we initially  
185 impose no balance, such that the (imbalanced) Coriolis and friction forces are the only ones acting

186 on the wind profile:

$$\begin{aligned}\frac{\partial U}{\partial t} &= fV + F_x[U, V] \\ \frac{\partial V}{\partial t} &= -fU + F_y[U, V]\end{aligned}\tag{6}$$

187 Combining (5) and (6) we see that the required PPGF to enforce geotriptic balance is simply the  
188 *negative* of the time tendency of the horizontal wind components, which can be estimated from  
189 their change after the first time step of model integration:

$$\begin{aligned}PPGF_x &= -fV - F_x[U, V] = -\frac{\partial U}{\partial t} \approx -\frac{U_f - U_i}{\Delta t} \\ PPGF_y &= fU - F_y[U, V] = -\frac{\partial V}{\partial t} \approx -\frac{V_f - V_i}{\Delta t}\end{aligned}\tag{7}$$

190 where the subscripts for  $U$  and  $V$  indicate the initial and final values for each model time step, and  
191  $\Delta t$  is the duration of the model time step. We calculate (7) at each vertical grid level in a column  
192 well removed from the initial storm-induced perturbations, or at each column in a given region  
193 and then taking a horizontal average. The result is the vertical PPGF profile that is then applied  
194 uniformly as an additional source term in the prognostic horizontal momentum equation at all grid  
195 columns for the remainder of the simulation. In practice we have found that the balance provided  
196 by this initial vertical PPGF profile is occasionally slightly upset during the first few minutes of  
197 model integration, possibly due to the effects of the initial development of subgrid-scale TKE.  
198 Testing (not shown) has revealed that continuously updating the PPGF profile after each time step  
199 for the first 300 s or so is sufficient to compensate for this effect. That is, after each time step for  
200 the first 300 s, we compute the new PPGF as:

$$PPGF_{(x,y)}(t_f) = PPGF_{(x,y)}(t_i) - \frac{(U, V)_f - (U, V)_i}{\Delta t}\tag{8}$$

201 where the last term on the RHS now represents the residual u- or v-momentum time-tendency  
202 not accounted for by the PPGF computed in the previous time step. Before the calculation of the  
203 PPGF at the first time step, it is initialized to zero so that (7) is recovered. With the estimated

204 PPGF included in the model, the wind profile is expected to remain quasi-steady in time away  
205 from storm-induced perturbations.

206 Whereas R16 finds an *adjusted* wind profile that is consistent with a geotriptic balance between  
207 the model friction force, the Coriolis, and a PPGF specified via an initial *geostrophic* balance, the  
208 GWB method works the other way and computes a PPGF that is in geotriptic balance with Coriolis  
209 and friction for a given *fixed* wind profile. At least for applications that require or benefit from  
210 control over the environmental wind profile, this ability to enforce geotriptic balance for any given  
211 initial wind profile is the new method's chief advantage over the R16 method. Moreover, the final  
212 adjusted wind profile in the R16 method will change as a function of details of the model friction  
213 parameterization, such as the value of the surface drag coefficient, whereas in the GWB method,  
214 the computed PPGF will change instead to compensate and maintain the same wind profile. In  
215 this regard, the GWB method is similar to the WC82 method, in that both effectively remove the  
216 influence of the surface friction on the environmental wind profile while still incorporating its  
217 effects on storm-induced perturbations. The chief advantage of the GWB method over WC82 is  
218 that it additionally balances the effects of friction *above the surface*, which may be substantial in  
219 some cases.

220 Finally, both the GWB and M16 methods work by adding an additional artificial forcing term to  
221 the RHS of the model momentum equations. In M16, the forcing term is a Newtonian relaxation  
222 (or nudging) term that increases in magnitude the more the horizontally averaged wind field differs  
223 from the reference profile. In contrast, in the simplest configuration of the GWB method (after the  
224 initial 300-s adjustment period) this term is constant in time and there is no forced relaxation  
225 toward a reference wind profile, which simplifies interpretation of the results. In this regard,  
226 our method is reminiscent of that of Nowotarski et al. (2015) who also added artificial forcing  
227 terms to the model momentum equations (as well as the potential temperature and water vapor

228 conservation equations). The forcing terms in their study were also only a function of height and  
229 were computed from the horizontal and time-averaged change in these variables over a 2-h period  
230 in a separate "stormless" simulation that included the growth of a realistic convective boundary  
231 layer. The goals of Nowotarski et al. (2015) and the current study are different, however, as they  
232 were concerned with the evolution of simulated storms in an *evolving* environment, whereas we  
233 again are concerned with how to maintain a *fixed* environment for simulated storms while still  
234 accounting for the effects of surface friction. Nevertheless, we adopt a very similar approach to  
235 initialize our supercell simulations with a turbulent boundary layer, where we additionally make  
236 use of a time-varying PPGF (see section 3d).

### 237 **3. Application of the GWB method to idealized supercell simulations**

#### 238 *a. Overview*

239 Next, we explore the utility of the GWB method through a series of idealized simulations of a  
240 strongly tornadic supercell and its environment using the Bryan Cloud Model, release 18.2 (CM1;  
241 Bryan and Fritsch 2002). We initialized the simulations using a sounding derived from the RUC  
242 model that was representative of the inflow environment of the tornadic supercells of the 24 May  
243 2011 Central Oklahoma tornado outbreak (Fig. 1; Orf et al. 2017, Wicker 2017, personal com-  
244 munication). The model domain is  $200 \times 200 \times 20 \text{ km}^3$  with a horizontal grid spacing of 250 m in  
245 an inner  $100 \times 100 \text{ km}^2$  region (hereafter the "inner domain") and gradually stretched to 1 km at  
246 the lateral boundaries. The surrounding outer stretched region of grid points is intended to pro-  
247 vide a larger area to minimize undesired lateral boundary condition effects, as well as to serve  
248 as a zone where turbulent eddies can be excited (see section 3d) before entering the inner high-  
249 resolution domain. A stretched vertical grid is imposed with 53 levels with spacing from 20 m

250 near the surface to 800 m at the model top. The domain translates with a constant  $[u,v] = [14.2,$   
251  $12.1]$   $\text{m s}^{-1}$  to keep the simulated storm near the center of the domain (though the Coriolis and  
252 frictional forces still act on the original ground-relative winds). To initiate convection, we use  
253 the updraft nudging technique of Naylor and Gilmore (2012) within an ellipsoidal region of radii  
254  $10 \times 10 \times 1.5$  km, centered at  $x = 100$  km,  $y = 100$  km, and  $z = 1.5$  km. The maximum magnitude of  
255 the nudging is  $10 \text{ m s}^{-1}$  and is applied over the first 900 s of the model integration. We employed  
256 the triple-moment version of the NSSL microphysics scheme (Mansell 2010; Dawson et al. 2014)  
257 and a 1.5-order prognostic TKE subgrid turbulence closure method based on Deardorff (1980).  
258 All simulations included the horizontal components of the Coriolis force with a constant Coriolis  
259 parameter  $f = 1 \times 10^{-4} \text{ s}^{-1}$ ; those simulations with the GWB method applied the Coriolis force  
260 to the full winds, while all others applied it to the perturbation winds only (i.e., assumed an initial  
261 large-scale geostrophic balance). We divide our experiments into sets with the following naming  
262 convention: [S, NS]-[T, NT]-[D, ND]-[GEO, GWB, WC], where we apply all combinations of  
263 each term in brackets for a total of 20 simulations. We describe each of the terms in the brackets  
264 in Table 1 and in detail in the following sections.

### 265 *b. Simulation of the environmental wind profile evolution in the absence of convection*

266 We first performed a set of simulations with no initial updraft forcing (“no-storm” or NS) and  
267 without resolved turbulence in the boundary layer (“no-turbulence” or NT). The goal of these  
268 experiments is to test the GWB method in the absence of storm-induced perturbations. This se-  
269 ries contained simulations with and without surface drag (D and ND, respectively), and with and  
270 without the GWB method applied: NS-NT-D-GEO, NS-NT-ND-GEO, NS-NT-D-GWB, and NS-  
271 NT-ND-GWB. Additionally, we performed a simulation with surface drag but applying the WC82  
272 base-state drag subtraction method: NS-NT-D-WC. Each simulation was integrated for 4 h. In

273 the experiments that included surface drag, it was parameterized by the introduction of horizontal  
 274 momentum stresses at the ground level as in R16:

$$-\tau_{13}(z=0) = \rho C_d V_h u, \quad (9)$$

275

$$-\tau_{23}(z=0) = \rho C_d V_h v, \quad (10)$$

276 where  $\tau_{13}$  and  $\tau_{23}$  are the subgrid-scale stress tensor components associated with the turbulent flux  
 277 of zonal  $u$  and meridional  $v$  (ground-relative) momentum, respectively,  $V_h$  is the ground-relative  
 278 horizontal wind speed, and  $C_d$  is the dimensionless drag coefficient which is set to a constant value  
 279 of 0.01 in each of the experiments with surface drag. For the GWB experiments, the PPGF profile  
 280 was calculated using the grid-cell area-weighted horizontal domain average of the time-tendency  
 281 of the horizontal momentum components. Again, the PPGF profile was updated each time step for  
 282 the first 300 s of the simulation to account for the initial development of subgrid-scale turbulence  
 283 and its early effect on the wind and thermodynamic profiles (not shown), and held fixed thereafter.

284 We show the temporal evolution of the low-level wind profile (horizontally averaged over the  
 285 inner domain) for each of the NS-NT- experiments in Fig. 2. Turning to the experiments without  
 286 surface drag first, NS-NT-ND-GEO (Fig. 2d) imposes an initial large-scale geostrophic balance,  
 287 while NS-NT-ND-GWB (Fig. 2e) additionally balances against the effects of internal mixing on  
 288 the profile. NS-NT-ND-GEO shows only small changes in the wind profile over time, mainly in a  
 289 slight reduction in the wind speed near the surface (see circles in (Fig. 2d)) and in a straightening of  
 290 the hodograph between 500-1000 m AGL (hodograph segment between X and star markers in Fig.  
 291 2d), while changes in NS-NT-ND-GWB are barely noticeable (Fig. 2e). The minor changes to the  
 292 hodograph in NS-NT-ND-GEO reflect the subtle action of internal subgrid-scale turbulent mixing  
 293 on the wind profile; the fact that these changes are relatively small confirms that the internal mixing

294 by itself has minimal effect, at least for this particular wind profile and subgrid-scale turbulence  
295 parameterization.

296 The experiments with surface drag, in contrast, show substantial differences in the evolution  
297 of the near surface wind profile. The hodograph evolution in NS-NT-D-GEO (Fig. 2a) differs  
298 substantially from that in NS-NT-D-GWB (Fig. 2b). The near-surface hodograph (i.e., below 1  
299 km AGL) in NS-NT-D-GEO lengthens substantially over time owing to a reduction in the near  
300 surface wind speed by the action of the surface drag. A similar effect is seen in the adjustment  
301 to the 3 May 1999 hodograph in R16 when they ran the original wind profile through a 1-D  
302 simulation that creates a steady-state balanced sounding (their Fig. 1). It can be inferred that  
303 the wind profile that a simulated storm "sees" will differ in potentially important ways from the  
304 initial environment if no balance procedure is employed in the presence of surface drag. On the  
305 other hand, in NS-NT-D-GWB, the wind profile remains nearly constant in time, as desired (Fig.  
306 2b). Finally, the NS-NT-D-WC hodograph evolution is very similar to that of NS-NT-D-GWB,  
307 except again for a slight reduction in the wind speeds just above the surface (Fig. 2c, circles) and a  
308 straightening of the hodograph between 500-1000 m AGL (Fig. 2c, hodograph segment between  
309 X and star markers), This represents a slight weakening of the shear in the lowest couple hundred  
310 meters relative to the initial profile. This behavior is nearly identical to that in NS-NT-ND-GEO  
311 (Fig. 2d, circles) and is due to the WC82 method only "balancing" the effects of the drag at the  
312 first level above the surface; the GWB method balances against the effects of surface drag and  
313 turbulent mixing throughout the entire profile.

### 314 *c. Supercell storm simulations*

315 We then performed a corresponding set of simulations, this time with early updraft forcing in-  
316 cluded but again with no resolved boundary layer turbulence (the S-NT- simulations). The updraft

317 forcing was applied starting at 300 s—just after the initial PPGF profile adjustment period to avoid  
318 contaminating the PPGF profile with the effects of storm-induced perturbations—and ending at  
319 1200 s into the simulation. In each simulation, an intense supercell storm formed with a maximum  
320 updraft near  $80 \text{ m s}^{-1}$  (Fig. 3a) and persisted for 3+ h, producing multiple intense tornado-strength  
321 vortices with maximum surface vorticity and wind speeds exceeding  $1 \text{ s}^{-1}$  and  $100 \text{ m s}^{-1}$  in some  
322 cases (Fig. 3b, c, respectively). (Transient updrafts reaching  $140+ \text{ m s}^{-1}$  in Fig. 3a are associ-  
323 ated with intensification of the vortices either at the surface or aloft). However, after 3 h, there  
324 was a tendency for the storm in each simulation to begin to lose supercell characteristics, as other  
325 cells that developed nearby began to merge their outflow with the primary cell, leading to upscale  
326 growth (not shown). For this reason we will only concern ourselves with the model output out  
327 to 3 h. As will be discussed in section 3d, the structure and behavior of the simulated storms,  
328 particularly near the surface, were substantially different between the simulations.

329 Similar to the NS-NT- experiments, we plot the hodograph evolution for the set of storm simula-  
330 tions in Fig. 4. In this case, however, we computed the hodographs from a horizontal average of the  
331 horizontal wind components in a  $20 \times 20 \text{ km}^2$  area at the southeast corner of the inner 250-m mesh,  
332 considered to be representative of the "far-field" inflow environment outside of the region most  
333 affected by storm-induced perturbations. If the GWB method is working well, we would expect  
334 this region far from the storm to show very limited modification over the period of the simulation  
335 similar to the corresponding "no-storm" case. As a comparison of Figs. 2 and 4 shows, there are  
336 still impacts from the storm visible in the far-field profile evolution, especially at the later times for  
337 S-NT-ND-GEO and S-NT-ND-GWB (Fig. 4d, e, respectively). Nevertheless, these are minor, and  
338 the GWB method clearly maintains a quasi-steady far-inflow wind profile for out to 3 h (Fig. 4b,  
339 e), as desired. The S-NT-D-WC experiment also exhibits a relatively steady wind profile (Fig. 4c),  
340 though not as steady as S-NT-D-GWB (Fig. 4b). The fact that the GWB method can preserve the

341 initial wind profile with only limited modification in the *far inflow* environment while still allow-  
342 ing the environment closer to the storm to evolve appropriately is clearly an advantage for studies  
343 that wish to systematically investigate the behavior of storms in a pre-specified/user-defined shear  
344 environment.

345 *d. Resolved versus subgrid-scale turbulence with the GWB method*

346 Markowski and Bryan (2016) compared LES-scale simulations of atmospheric boundary lay-  
347 ers with and without resolved-scale turbulent structures. They demonstrated that when the initial  
348 environmental flow is laminar (that is, does not contain appreciable turbulent structures that are  
349 resolved on the grid), common LES turbulent closure assumptions tend to overestimate the amount  
350 of shear in the surface layer. In their simulations where resolved turbulence was activated via the  
351 introduction of random perturbations to the initial state that were then recycled through the peri-  
352 odic boundaries, the near-surface shear was reduced, as was the fraction of TKE partitioned into  
353 the subgrid-scale parameterization. This issue potentially has implications for the interpretation  
354 of the effects of surface drag on a wide range of simulated storm behavior, and we refer the reader  
355 to Markowski and Bryan (2016) for details. For our purposes, when resolved turbulent structures  
356 are present in the pre-storm boundary-layer environment, the environmental wind profile is clearly  
357 no longer even approximately horizontally homogeneous. Yet, there still may be a desire to main-  
358 tain the *horizontal mean* profile in the same way as when the pre-storm environment is laminar.  
359 To demonstrate the utility of the GWB method for this situation, we perform and analyze two  
360 additional sets of experiments in which the boundary layer contains resolved turbulent structures.

361 We first discuss the NS-T- experiments—analogueous to the NS-NT- experiments but including  
362 a field of resolved turbulent structures in the boundary layer. Our main purpose is to analyze the  
363 impact of resolved turbulence on the average environmental wind profile for the same experimental

364 setup as the original NS-NT- experiments (that is, without storm-induced perturbations). Our  
365 method for encouraging the development of turbulence is similar to the "point" method of Muñoz-  
366 Esparza et al. (2014). We apply random uniformly distributed potential temperature perturbations  
367 of +/- 0.25 K to the initial conditions, as well as every 200 s during the model integration to  
368 a 20-grid point-wide zone positioned 40 grid points from each inflow boundary. We apply the  
369 perturbations from the surface up to 1 km AGL, the approximate depth of the boundary layer in  
370 this case. This mechanism leads to well-developed turbulent structures in the boundary layer by  
371 approximately 1-2 h, which continue to grow in intensity until the end of the simulation (Fig. 5).  
372 That is, the turbulence never reaches a statistically steady state, though we don't consider this to  
373 be detrimental to our goal, which is to understand the impact on the wind profile in a qualitative  
374 sense. Future work may focus on developing a more robust methodology for generating a turbulent  
375 boundary layer in a statistically steady state with a given mean wind profile, perhaps by using  
376 an "eddy injection" method similar to Bryan et al. (2017). Because the resolved turbulence is  
377 changing in intensity with time, for the two experiments where we applied the GWB method—  
378 NS-D-GWBT- and NS-ND-GWBT—we update the PPGF profile every time step throughout the  
379 simulation, instead of only the first 300 s as in the NS-T- experiments. Again, we use the grid-  
380 area weighted domain horizontal average of the horizontal momentum time tendencies to compute  
381 the PPGF profile, which effectively removes the effect of small-scale fluctuations owing to the  
382 turbulent eddies.

383 In Fig. 6, we show vertical profiles valid at 2 h of the subgrid-scale vs. resolved turbulence  
384 kinetic energy (TKE), horizontally averaged over the inner domain, for each corresponding pair of  
385 experiments without (NS-NT-) and with (NS-T-) resolved BL turbulence (left and right columns,  
386 respectively). Resolved TKE was computed according to  $TKE = 0.5\sqrt{u'^2 + v'^2 + w'^2}$ , where the  
387 primes represent departures from the domain horizontal averages of each of the three wind com-

388 ponents. Consistent with the results of Markowski and Bryan (2016), the NS-NT- experiments  
389 contain virtually no resolved TKE, while the NS-T- experiments have a substantial portion of the  
390 total TKE taken up by the resolved flow. For each of the experiments without parameterized sur-  
391 face drag (the -ND-GEO and -ND-GWB experiments), the surface layer exhibits relatively small  
392 magnitudes of either resolved or subgrid-scale TKE, as expected (Fig. 6g, h, i, j). In contrast, in  
393 the experiments with surface drag (-D-GEO, -D-WC and -D-GWB), the subgrid-scale TKE in the  
394 surface layer is much larger than anywhere else in the profile (Fig. 6c, d, e, f) owing to the large as-  
395 sumed surface drag-induced shear in the lowest 10-m (below the lowest height at which the model  
396 horizontal wind components are valid). It is this large surface layer subgrid-scale turbulence that  
397 is directly responsible for the rapid weakening of the near-surface winds in the experiments that  
398 included surface drag but only initial geostrophic balance (NS-NT-D-GEO and NS-T-D-GEO; c.f.  
399 2a and 7a). By 2 h, owing to these reduced surface winds, the amount of subgrid-scale turbulence  
400 in the surface layer is correspondingly reduced in both of these experiments (Fig. 6a) as compared  
401 to any of the experiments where the surface drag was balanced (Fig. 6c-f).

402 When the GWB method is not active (i.e. in the GEO and WC experiments), the presence  
403 or absence of boundary layer turbulence has only modest effects on the overall evolution of the  
404 wind profile, despite the large differences in the vertical profiles of TKE between corresponding  
405 pairs (compare left and right columns of Fig. 6). However, there is slightly more modification  
406 of the hodograph between 500 m and 1000 m in the non-GWB turbulent BL experiments (Fig.  
407 7a, c, d) than in the corresponding non-turbulent BL experiments (Fig. 2a, c, d). This additional  
408 modification can be explained by the addition of substantial resolved TKE maximized near 500 m  
409 AGL in the turbulent-BL runs (Fig. 6 right column), but with the subgrid-scale TKE remaining  
410 nearly the same as in their non-turbulent BL counterparts (Fig. 6 left column).

411 When the GWB method is active and surface drag is present, the surface drag is balanced by a  
412 strong PPGF (Fig. 8 red line near the surface). Above this shallow surface layer (or throughout the  
413 profile for the runs without surface drag; blue lines), the magnitude of the PPGF is much lower and  
414 its profile differs between the turbulent and non-turbulent BL simulations (Fig. 8a). In particular,  
415 the turbulent-BL simulations show less southward-directed (or more northward-directed) PPGF in  
416 the turbulent runs (dashed lines) than the non-turbulent runs (solid lines), indicating a tendency for  
417 the resolved turbulent mixing in this portion of the profile to weaken the meridional winds more  
418 than in the non-turbulent simulations (Fig. 8b). In the non-turbulent simulations, the PPGF and  
419 Coriolis are nearly balanced above approximately 200 m AGL (compare solid lines with dotted  
420 black line in Fig. 8a). Between about 100-200 m, both subgrid-scale and resolved mixing are  
421 instantaneously acting to weaken the shear in this layer by increasing the meridional winds from  
422 50-100 m and decreasing them above (Fig. 8b). The PPGF counters these tendencies in order to  
423 maintain the wind profile (and thus the shear) in this layer (Fig. 8a).

424 Otherwise, the fact that the differences are relatively minor between the turbulent and non-  
425 turbulent-BL simulations can be explained by the overall small forcing from the TKE (either re-  
426 solved or subgrid) on the overall wind profile above the shallow surface layer and the fact that the  
427 surface layer is completely dominated by the subgrid-scale TKE, as expected in LES-type simula-  
428 tions (see Markowski and Bryan 2016, and references therein). We think it is plausible, however,  
429 that different wind profiles may exhibit somewhat different sensitivities, particularly when consid-  
430 ering the effects of the thermodynamic profile. For example, turbulence would be enhanced for  
431 large virtual temperature lapse rates and suppressed for small lapse rates.

432 Finally, we also performed a series of storm experiments—analogue to the S-NT- experiments—  
433 but with a turbulent boundary layer (the S-T- experiments). The initialization of these simulations  
434 as well as the application of the GWB method is somewhat more complicated than in the corre-

435 sponding S-NT- simulations. We desire to initiate storms in an environment where the boundary  
436 layer already has appreciable resolved turbulent structures. Therefore, we took the model output  
437 valid at 2 h from the no-storm GWB simulations (NS-T-D-GWB and NS-T-ND-GWB) and used  
438 them as the initial conditions for the appropriate sets of storm simulations (that is, with and without  
439 surface drag, respectively). Since as already discussed the GWB method ensured that the average  
440 wind profile was preserved in NS-T-D-GWB and NS-T-ND-GWB, this means that the new set of  
441 S-T- simulations all start with the same *average* environmental wind profile as those storm simu-  
442 lations *without* resolved BL turbulence (i.e the S-NT- simulations). This approach is very similar  
443 to that of Nowotarski et al. (2015) who likewise initialized their supercell storm simulations from  
444 a previous set of simulations of convective boundary layers with fully developed turbulence. In  
445 their simulations, however, it was difficult to maintain the average low-level vertical wind profile  
446 over the course of their storm simulations because of the lack of a large-scale PGF to balance  
447 the turbulent mixing (Nowotarski et al. 2014); the GWB method provides this as follows. Recall  
448 that the PPGF profile was continuously updated for the two no-storm GWB experiments (NS-T-  
449 D-GWB and NS-T-ND-GWB), such that the average wind profile remained constant even while  
450 the boundary layer turbulence continuously evolved (c.f. Fig. 5). For the two GWB storm exper-  
451 iments (S-T-D-GWB and S-T-ND-GWB) we used the PPGF profile valid at 2 h in NS-T-D-GWB  
452 and NS-T-ND-GWB, respectively, and then *held it fixed* for the duration of the two storm simu-  
453 lations. This ensures that in the horizontal mean, the PPGF profile balances the frictional force  
454 profile *at least at the initial time*. While we could have continued to update the PPGF profile in  
455 the face of the changing horizontal average of the horizontal momentum time-tendencies, as in  
456 the NS-T- experiments, in this case we would have been also compensating for the average of the  
457 *storm-induced perturbations* to the wind profile, which is undesirable for the present purposes.  
458 We show the wind profile evolution for the S-T- experiments in Fig. 9. Here, as in the storm simu-

459 lations without resolved turbulence (the S-NT- experiments), the profiles are taken as a horizontal  
460 average of a  $20 \times 20 \text{ km}^2$  area at the southeast corner of the inner 250-m mesh, to represent the  
461 far-inflow region (the  $20 \times 20 \text{ km}^2$  is sufficient to average out the effects of the resolved turbulence,  
462 not shown). The same basic evolution is seen when comparing the hodographs between pairs of  
463 experiments from the NS-T- (Fig. 7) and S-T- (Fig. 9) sets indicating that the presence of the storm  
464 does not substantially affect the far-inflow wind profile, and that GWB method reliably maintains  
465 it.

#### 466 **4. Impact of surface drag on simulated storm structure**

467 Finally, motivated by the aforementioned recent work on this problem, we turn to a brief anal-  
468 ysis of the impact of surface drag on simulated near-surface storm structure and behavior. As  
469 noted earlier, each simulation produced several intense tornado-strength vortices, with an overall  
470 increase in activity after  $\sim 2 \text{ h}$  (c.f. Fig. 3). As an initial foray, we wish to reveal any 1st-order  
471 differences in near-surface kinematic structure that persist over time across the simulations, since  
472 the near-surface wind field associated with the storm and attendant tornadoes would be expected  
473 to be most *directly* affected by the presence or absence of surface drag. To this end, we constructed  
474 temporal composites by tracking the location of maximum vertical vorticity within a  $12 \times 12 \text{ km}^2$   
475 moving box at 500 m AGL every 60 s during the second hour of each simulation and rejecting  
476 those times when the vertical vorticity decreased below  $0.1 \text{ s}^{-1}$ . Additionally, we rejected those  
477 times when the position of the vortex deviated more than 3 km from its median position of all  
478 the previous times; we found this to be necessary to avoid centering on spurious non-tornadic or  
479 vortices that had significant storm-relative rearward motion (i.e. "occluding" vortices). We then  
480 aligned the model fields in the horizontal at the individual times relative to the surface vortex  
481 location and performed a simple average across the times.

482 We show the resulting composites for surface horizontal wind speed (color fill), asymptotic  
483 contraction rate (ACR; green contours)<sup>1</sup>, and surface simulated radar reflectivity (dBZ; black con-  
484 tours) in Fig. 10. While we performed these composites for both the S-NT- and S-T- sets of  
485 experiments, the results were not substantially different in a qualitative sense, and thus we show  
486 only the S-NT- results for the sake of brevity. The presence or absence of surface drag profoundly  
487 alters the near-surface kinematic structure of the storm. First, the two experiments without sur-  
488 face drag (S-NT-ND-GEO and S-NT-ND-GWB; Fig. 10d, e) exhibit a large area of strong surface  
489 winds  $>20 \text{ m s}^{-1}$  up to 10 km from the vortex. In contrast, three experiments with surface  
490 drag (S-NT-D-GEO, S-NT-D-GWB, and S-NT-D-WC; Fig. 10a, b, c) all show the strongest winds  
491 in a much smaller area close to the simulated tornado.

492 The two simulations without surface drag also exhibit a much more prominent rear-flank gust  
493 front (RFGF) as well as a prominent boundary extending off to the northeast of the surface vortex  
494 into the forward flank of the storm that resembles the "left flank convergence boundary" (LFCB)  
495 identified in the simulations of Beck and Weiss (2013). In contrast, the simulations with surface  
496 drag have a less prominent boundary in the mean in the forward flank region. Moreover, the  
497 structure of the RFGF and its orientation relative to the surface vortex is quite different between  
498 the simulations with and without surface drag. In the no-drag simulations, the RFGF appears as  
499 a single entity (at least in the mean, as defined by the compositing procedure) that appears nearly  
500 contiguous with the LFCB/FFGF, both having a roughly SSW to NNE orientation (green contours  
501 in Fig. 10d, e). The simulated tornado in these simulations is located very near the intersection  
502 of these two boundaries with relatively little arcing of the RFGF. This structure is qualitatively  
503 very similar to that seen in several other published simulations of supercells that used free-slip

---

<sup>1</sup>This purely kinematic quantity is a measure of the long-term rate at which adjacent air parcels approach each other given a steady kinematic flow field, and is more useful for identifying airstream boundaries than simple divergence (Cohen and Schultz 2005; Betten et al. 2018)

504 lower boundary conditions (e.g, Adleman and Droegemeier 2002; Dahl et al. 2012; Beck and  
505 Weiss 2013). In contrast, in each of the three drag simulations, the RFGF forms a tightening  
506 cyclonic arc or spiral through at least 180 degrees, that wraps around the simulated tornado such  
507 that the latter is "tucked" into the tighter, western portion of the spiral or even kinematically  
508 "detached" from it (green contours in Fig. 10a-c). Except for perhaps S-NT-D-GWB, there is little  
509 evidence for a prominent forward flank boundary in the mean, although inspection of individual  
510 times (especially later in the simulation) indicate that the drag simulations do form several transient  
511 forward flank boundaries (not shown). This general forward- and rear-flank boundary structure  
512 is consistent with that found in several recent published simulations that included surface drag  
513 parameterizations (e.g., Schenkman et al. 2014, 2016; Dawson et al. 2015; Roberts et al. 2016;  
514 Coffey and Parker 2017; Coffey et al. 2017) and in observation-based studies (e.g., Skinner et al.  
515 2011; Lee et al. 2012; Marquis et al. 2012; Kosiba et al. 2012; Skinner et al. 2014). Additionally,  
516 the drag experiments all show another persistent boundary trailing SSW from the vortex itself.  
517 This boundary is roughly parallel with the eastern portion of the RFGF and separated from it  
518 by  $\sim 5$  km, and bears striking resemblance to the so-called "secondary rear flank gust front"  
519 or "internal momentum surge" identified in several recent modeling and observational analysis  
520 studies of tornadic supercells (e.g., Skinner et al. 2011; Lee et al. 2012; Schenkman et al. 2016;  
521 Marquis et al. 2012; Kosiba et al. 2012; Skinner et al. 2014). While the no-drag simulations also  
522 exhibit these secondary gust fronts, they are much more transient and thus do not show up in the  
523 composite fields.

524 Fig. 10 suggests that the overall kinematic structure of the storm at the surface, at least during  
525 times when the surface vortex is most intense, is not appreciably different between the GWB/WC  
526 and non-GWB simulations. However, the two experiments that balanced surface drag (S-NT-D-  
527 GWB and S-NT-D-WC ) have stronger southeasterly flow in the inflow region and weaker north-

528 westerly flow in the outflow region north of the surface vortex than is the case in the experiment  
529 that included both surface drag and only initial geostrophic balance (S-NT-D-GEO). This can be  
530 seen by comparing wind vectors in the corresponding regions in Fig. 10b, c with Fig. 10a).  
531 The weaker southeasterly inflow into the storm in S-NT-D-GEO is clearly due to the surface drag  
532 weakening the near-surface flow (c.f. hodograph Fig. 4a). The stronger environmental or back-  
533 ground southeasterly flow in S-NT-D-GWB and S-NT-D-WC apparently cancel out some of the  
534 northwesterly storm-induced outflow northwest of the low-level vortex center to produce weaker  
535 total ground relative winds there (compare wind vectors in the upper left quadrant of Fig. 10b, c  
536 with Fig. 10a). Additionally, the winds in the composite vortex in S-NT-D-WC (color filled region  
537 in Fig. 10c) are noticeably weaker than in the other two drag simulations (Fig. 10a, b); this is also  
538 evident in the timeseries of maximum horizontal wind speed (Fig. 3, blue line). The reason for  
539 this difference is unclear, but may be related to the somewhat weaker shear that develops with time  
540 in the lowest  $\sim 500$  m in the far-field inflow wind profile for this experiment (Fig. 4c, circle and  
541 x markers) as compared to S-NT-D-GEO and S-NT-D-GWB (Fig. 4a, b, respectively). A com-  
542 plete investigation into the reasons for these differences and a thorough comparison with previous  
543 simulations and observations is beyond the scope of this study but will be pursued in future work.

## 544 **5. Summary and Discussion**

545 We have developed a new method to to compute a large-scale pressure gradient for use within at-  
546 mospheric simulation models with idealized background environments. The method is particularly  
547 useful for idealized simulations of convection and other phenomena where it is desirable to pre-  
548 cisely control and maintain the large-scale kinematic environment while simultaneously including  
549 the effects of surface friction and "internal" friction aloft. A prime example are high-resolution  
550 supercell tornado simulations initialized from a single environmental sounding where satisfying

551 both of these conditions has historically proven difficult, owing to the tendency for surface fric-  
552 tion in particular to modify the low-level environmental wind profile over time in the absence of  
553 a large-scale balance that includes the frictional force. The primary appeal of the new method is  
554 its applicability to an arbitrary wind profile coupled with any given surface drag and turbulence  
555 formulation, including in the presence of resolved turbulent structures that evolve over time. The  
556 method is conceptually simple and easy to implement in existing models, and works by determin-  
557 ing the horizontal force as a function of height that is needed to cancel out the horizontal frictional  
558 and Coriolis forces. The method estimates this force profile as the negation of the time tendency  
559 of the horizontal momentum equations early in the simulation at each grid level in a suitable (i.e.  
560 perturbation free) column (or average of columns). This vertical force profile is then included as  
561 an additional term in the horizontal momentum equations for the duration of the simulation.

562 We demonstrated the method by applying it to a series of idealized simulations of a supercell  
563 using a sounding representative of the inflow environment of the storms in the 24 May 2011  
564 Oklahoma tornado outbreak. With the Geotriptic Wind Balance method, the far-field low-level  
565 wind profile remains essentially unchanged throughout the 3-4 h model integration, even with the  
566 presence of surface drag and/or resolved turbulent eddies. The simulations with resolved boundary  
567 layer turbulent eddies were (somewhat surprisingly) very similar in their overall behavior with  
568 their non-turbulent counterparts, though subtle differences in the evolution of the wind profiles did  
569 exist. Namely, there was a tendency for slightly more modification of the wind profile to occur over  
570 time when comparing corresponding experiments in the turbulent vs. the non-turbulent boundary  
571 layer sets in which the GWB method was not employed. In ongoing work we are investigating the  
572 sensitivity of simulated supercells and their attendant tornadoes to the presence of surface drag and  
573 resolved vs. subgrid-scale turbulence; as part of this effort we will continue to assess the utility of

574 the GWB method for other wind profiles and higher grid resolutions in which turbulent structures  
575 would be better resolved. Results of these investigations will be reported in a future paper.

576 While in this study we focused on the goal of controlling (via maintaining) a *fixed* background  
577 wind profile, the emphasis should be on the word "control" rather than "fixed". The GWB method  
578 can easily be generalized to control other aspects of the environmental evolution, and has similar-  
579 ity to some methods found in the published literature. Nolan and Rappin (2008) applied a fictitious  
580 force to the model horizontal momentum equations to maintain a time-invariant background ver-  
581 tical wind profile in order to investigate the effects of vertical wind shear in idealized simulations  
582 of tropical cyclones. Bryan et al. (2017) applied a similar method to maintain a time-invariant  
583 background flow that was in gradient wind balance in limited-area LES experiments to explore the  
584 wind profile in the tropical cyclone boundary layer. That is, they explicitly computed the required  
585 PPGF that would satisfy *gradient* wind balance rather than *geostrophic* as is more commonly used,  
586 and added this term to the model momentum equations in much the same manner as in the present  
587 study.

588 Other researchers have sought to examine in a controlled manner the impact of a *changing*  
589 background wind profile on simulated convective storm evolution. Letkewicz et al. (2013) used a  
590 method they dubbed "base-state substitution" where a simulation was performed with one kine-  
591 matic and thermodynamic profile defining the horizontally homogeneous base state, which was  
592 then replaced with another at some time during the simulation. A limitation of this approach is  
593 seemingly the abrupt nature in which the background profile changes. Using an approach more  
594 similar to our own, Kost and Richardson (2004) applied a time-varying fictitious force profile to  
595 the momentum equations that slowly modified the background wind profile from one state to an-  
596 other with stronger wind shear. Our method can easily be modified to perform this function while  
597 simultaneously including the effects of surface friction. Another potential application in this vein

598 would be for studying the effects of changing surface roughness within a single simulation, by  
599 interpolating over a short period the PPGF profiles that balance the frictional forces associated  
600 with two or more different values of the drag coefficient that are "activated" at specific times in  
601 the simulation. Furthermore, our method is not limited to convective storm or tropical cyclone  
602 simulations; it can be applied to, for example, idealized orographic flow simulations that include  
603 surface frictional effects. The same procedure can be used to help maintain the upstream wind  
604 profile that eventually flows over the mountain.

605 *Acknowledgments.* The authors wish to thank Dr. Chris Nowotarski and two other anonymous  
606 reviewers for their comments which greatly improved the quality of the manuscript. We are grate-  
607 ful for the many fruitful discussions with colleagues regarding this work, including Drs. Johannes  
608 Dahl, Paul Markowski, Yvette Richardson, Lou Wicker, Ted Mansell, George Bryan, Brice Coffey,  
609 Patrick Skinner, Robin Tanamachi, and Corey Potvin, among many others. We also acknowledge  
610 Dr. George Bryan for his continued support of the CM1 model. Most of the post-processing and  
611 plotting of the simulation output was carried out using the Python programming language and  
612 leveraged numerous open-source modules, most notably the MetPy (May et al. 2008 - 2017) and  
613 matplotlib (Hunter 2007) packages. Support for this work came from the first author's institution  
614 in the form of start-up funding.

## 615 **References**

616 Adlerman, E. J., and K. K. Droegemeier, 2002: The Sensitivity of Numerically Simulated  
617 Cyclic Mesocyclogenesis to Variations in Model Physical and Computational Parameters.  
618 *Monthly Weather Review*, **130** (11), 2671–2691, doi:10.1175/1520-0493(2002)130<2671:  
619 TSONSC>2.0.CO;2, URL [http://ams.allenpress.com/perlserv/?request=get-abstract&doi=10.](http://ams.allenpress.com/perlserv/?request=get-abstract&doi=10.1175/1520-0493(2002)130<2671:TSONSC>2.0.CO;2)

620 1175/1520-0493(2002)130<2671:TSONSC>2.0.CO;2[http://journals.ametsoc.org/doi/abs/10.1175/1520-0493\(2002\)130<2671:TSONSC>2.0.CO;2](http://journals.ametsoc.org/doi/abs/10.1175/1520-0493(2002)130<2671:TSONSC>2.0.CO;2).

621 1175/1520-0493(2002)130<2671:TSONSC>2.0.CO;2.

622 Beck, J. R., and C. C. Weiss, 2013: An Assessment of Low-Level Baroclinity and Vortic-  
623 ity within a Simulated Supercell. *Monthly Weather Review*, **141** (2), 649–669, doi:10.1175/  
624 MWR-D-11-00115.1, URL <http://journals.ametsoc.org/doi/abs/10.1175/MWR-D-11-00115.1>.

625 Betten, D. P., M. I. Biggerstaff, and C. L. Ziegler, 2018: Three-Dimensional Storm Structure  
626 and Low-Level Boundaries at Different Stages of Cyclic Mesocyclone Evolution in a High-  
627 Precipitation Tornadoic Supercell. *Advances in Meteorology*, **2018** (Article ID 9432670), 1–24,  
628 doi:10.1155/2018/9432670.

629 Bryan, G. H., and J. M. Fritsch, 2002: A Benchmark Simulation for Moist Nonhydro-  
630 static Numerical Models. *Monthly Weather Review*, **130** (1992), 2917–2928, doi:10.1175/  
631 1520-0493(2002)130<2917:ABSFMN>2.0.CO;2, URL [http://journals.ametsoc.org/doi/abs/10.1175/1520-0493\(2002\)130<2917:ABSFMN>2.0.CO;2](http://journals.ametsoc.org/doi/abs/10.1175/1520-0493(2002)130<2917:ABSFMN>2.0.CO;2).

632 1175/1520-0493(2002)130<2917:ABSFMN>2.0.CO;2.

633 Bryan, G. H., R. P. Worsnop, J. K. Lundquist, and J. A. Zhang, 2017: A Simple Method for Simu-  
634 lating Wind Profiles in the Boundary Layer of Tropical Cyclones. *Boundary-Layer Meteorology*,  
635 **162** (3), 475–502, doi:10.1007/s10546-016-0207-0.

636 Coffey, B. E., and M. D. Parker, 2017: Simulated Supercells in Nontornadoic and Tor-  
637 nadoic VORTEX2 Environments. *Monthly Weather Review*, **145** (1), 149–180, doi:10.1175/  
638 MWR-D-16-0226.1, URL <http://journals.ametsoc.org/doi/10.1175/MWR-D-16-0226.1>.

639 Coffey, B. E., M. D. Parker, J. M. L. Dahl, L. J. Wicker, and A. J. Clark, 2017: Volatility of  
640 Tornadoogenesis: An Ensemble of Simulated Nontornadoic and Tornadoic Supercells in VORTEX2

641 Environments. *Monthly Weather Review*, **145** (11), 4605–4625, doi:10.1175/MWR-D-17-0152.  
642 1, URL <http://journals.ametsoc.org/doi/10.1175/MWR-D-17-0152.1>.

643 Cohen, R. A., and D. M. Schultz, 2005: Contraction Rate and Its Relationship to Frontogenesis,  
644 the Lyapunov Exponent, Fluid Trapping, and Airstream Boundaries. *Monthly Weather Review*,  
645 (133), 1353–1369.

646 Dahl, J. M. L., M. D. Parker, and L. J. Wicker, 2012: Uncertainties in Trajectory Calcula-  
647 tions within Near-Surface Mesocyclones of Simulated Supercells. *Monthly Weather Review*,  
648 **140** (9), 2959–2966, doi:10.1175/MWR-D-12-00131.1, URL <http://journals.ametsoc.org/doi/abs/10.1175/MWR-D-12-00131.1>.

650 Davies-Jones, R. P., 2014: A review of supercell and tornado dynamics. *Atmospheric Re-*  
651 *search*, **158-159**, 1–18, doi:10.1016/j.atmosres.2014.04.007, URL <http://linkinghub.elsevier.com/retrieve/pii/S0169809514001756>.

653 Dawson, D. T., E. R. Mansell, Y. Jung, L. J. Wicker, M. R. Kumjian, and M. Xue, 2014: Low-  
654 Level  $\{Z_{DR}\}$  Signatures in Supercell Forward Flanks: The Role of Size Sorting and Melt-  
655 ing of Hail. *Journal of the Atmospheric Sciences*, **71**, 276–299, doi:[http://dx.doi.org/10.1175/](http://dx.doi.org/10.1175/JAS-D-13-0118.1)  
656 [JAS-D-13-0118.1](http://dx.doi.org/10.1175/JAS-D-13-0118.1).

657 Dawson, D. T., M. Xue, J. a. Milbrandt, and A. Shapiro, 2015: Sensitivity of Real-Data Sim-  
658 ulations of the 3 May 1999 Oklahoma City Tornadic Supercell and Associated Tornadoes to  
659 Multimoment Microphysics. Part I: Storm- and Tornado-Scale Numerical Forecasts. *Monthly*  
660 *Weather Review*, **143** (6), 2241–2265, doi:10.1175/MWR-D-14-00279.1, URL <http://journals.ametsoc.org/doi/abs/10.1175/MWR-D-14-00279.1>.

661

662 Deardorff, J. W., 1980: Stratocumulus-capped mixed layers derived from a three-dimensional  
663 model. *Boundary-Layer Meteorology*, **18** (4), 495–527, doi:10.1007/BF00119502.

664 Fiedler, B. H., and R. Rotunno, 1986: A Theory for the Maximum Windspeeds in Tornado-  
665 like Vortices. *Journal of the Atmospheric Sciences*, **43** (21), 2328–2340, doi:10.1175/  
666 1520-0469(1986)043<2328:ATOTMW>2.0.CO;2, URL [http://journals.ametsoc.org/doi/abs/10.  
667 1175/1520-0469\(1986\)043<2328:ATOTMW>2.0.CO;2](http://journals.ametsoc.org/doi/abs/10.1175/1520-0469(1986)043<2328:ATOTMW>2.0.CO;2).

668 Hunter, J. D., 2007: Matplotlib: A 2d graphics environment. *Computing In Science & Engineering*,  
669 **9** (3), 90–95, doi:10.1109/MCSE.2007.55.

670 Johnson Jr, W., 1966: The “geotriptic wind”. *Bull. Amer. Meteor. Soc*, **47** (982), 167.

671 Klemp, J. B., and R. B. Wilhelmson, 1978: The Simulation of Three-Dimensional  
672 Convective Storm Dynamics. *Journal of the Atmospheric Sciences*, **35** (6), 1070–  
673 1096, doi:10.1175/1520-0469(1978)035<1070:TSOTDC>2.0.CO;2, URL [http://journals.  
674 allenpress.com/jrnlserv/?request=get-abstract&issn=1520-0469&volume=35&page=1070http:  
675 //journals.ametsoc.org/doi/abs/10.1175/1520-0469\(1978\)035<1070:TSOTDC>2.0.CO;2](http://journals.allenpress.com/jrnlserv/?request=get-abstract&issn=1520-0469&volume=35&page=1070http://journals.ametsoc.org/doi/abs/10.1175/1520-0469(1978)035<1070:TSOTDC>2.0.CO;2).

676 Kosiba, K., J. M. Wurman, Y. P. Richardson, P. M. Markowski, P. Robinson, and J. Marquis, 2012:  
677 Genesis of the Goshen County, Wyoming Tornado on 05 June 2009 during VORTEX2. *Monthly  
678 Weather Review*, (June 2009), 120914093304 006, doi:10.1175/MWR-D-12-00056.1.

679 Kost, J., and Y. P. Richardson, 2004: The influence of temporally-varying vertical wind shear on  
680 numerically simulated convective storms. *22nd Conference on Severe Local Storms*, American  
681 Meteorological Society, Hyannis, MA, 9.2.

682 Lee, B. D., C. a. Finley, and C. D. Karstens, 2012: The Bowdle, South Dakota, Cyclic Tor-  
683 nadic Supercell of 22 May 2010: Surface Analysis of Rear-Flank Downdraft Evolution and

- 684 Multiple Internal Surges. *Monthly Weather Review*, (May 2010), 120622135912 009, doi:  
685 10.1175/MWR-D-11-00351.1.
- 686 Letkewicz, C. E., A. J. French, and M. D. Parker, 2013: Base-State Substitution: An Idealized  
687 Modeling Technique for Approximating Environmental Variability. *Monthly Weather Review*,  
688 **141 (9)**, 3062–3086, doi:10.1175/MWR-D-12-00200.1, URL [http://journals.ametsoc.org/doi/  
689 abs/10.1175/MWR-D-12-00200.1](http://journals.ametsoc.org/doi/abs/10.1175/MWR-D-12-00200.1).
- 690 Lewellen, D. C., and W. S. Lewellen, 2007: Near-Surface Intensification of Tornado Vortices.  
691 *Journal of the Atmospheric Sciences*, **64 (7)**, 2176–2194, doi:10.1175/JAS3965.1.
- 692 Loftus, A. M., D. B. Weber, and C. A. Doswell, 2008: Parameterized Mesoscale Forcing Mecha-  
693 nisms for Initiating Numerically Simulated Isolated Multicellular Convection. *Monthly Weather*  
694 *Review*, **136 (7)**, 2408–2421, doi:10.1175/2007MWR2133.1, URL [http://dx.doi.org/10.1175/  
695 2007MWR2133.1](http://dx.doi.org/10.1175/2007MWR2133.1).
- 696 Mansell, E. R., 2010: On Sedimentation and Advection in Multimoment Bulk Microphysics.  
697 *Journal of the Atmospheric Sciences*, **67 (9)**, 3084–3094, doi:10.1175/2010JAS3341.1, URL  
698 <http://journals.ametsoc.org/doi/abs/10.1175/2010JAS3341.1>.
- 699 Markowski, P. M., 2016: An idealized numerical simulation investigation of the effects of sur-  
700 face drag on the development of near-surface vertical vorticity in supercell thunderstorms.  
701 *Journal of the Atmospheric Sciences*, 16–0150, doi:10.1175/JAS-D-16-0150.1, URL [http:  
702 //journals.ametsoc.org/doi/10.1175/JAS-D-16-0150.1](http://journals.ametsoc.org/doi/10.1175/JAS-D-16-0150.1).
- 703 Markowski, P. M., and G. H. Bryan, 2016: LES of Laminar Flow in the PBL: A Potential Problem  
704 for Convective Storm Simulations. *Monthly Weather Review*, **144 (5)**, 1841–1850, doi:10.1175/  
705 MWR-D-15-0439.1, URL <http://journals.ametsoc.org/doi/10.1175/MWR-D-15-0439.1>.

706 Marquis, J., Y. P. Richardson, P. M. Markowski, D. C. Dowell, and J. M. Wurman, 2012:  
707 Tornado Maintenance Investigated with High-Resolution Dual-Doppler and EnKF Analy-  
708 sis. *Monthly Weather Review*, **140** (1), 3–27, doi:10.1175/MWR-D-11-00025.1, URL <http://journals.ametsoc.org/doi/abs/10.1175/MWR-D-11-00025.1>.  
709

710 Mashiko, W., 2016: A Numerical Study of the 6 May 2012 Tsukuba City Supercell Tornado. Part  
711 II: Mechanisms of Tornadogenesis. *Monthly Weather Review*, **144** (9), 3077–3098, doi:10.1175/  
712 MWR-D-15-0122.1, URL <http://journals.ametsoc.org/doi/10.1175/MWR-D-15-0122.1>.

713 May, R., S. Arms, P. Marsh, E. Bruning, and J. Leeman, 2008 - 2017: Metpy: A Python package  
714 for meteorological data. Boulder, Colorado, URL <https://github.com/Unidata/MetPy>, doi:10.  
715 5065/D6WW7G29.

716 Muñoz-Esparza, D., B. Kosović, J. Mirocha, and J. van Beeck, 2014: Bridging the Transition from  
717 Mesoscale to Microscale Turbulence in Numerical Weather Prediction Models. *Boundary-Layer*  
718 *Meteorology*, **153** (3), 409–440, doi:10.1007/s10546-014-9956-9.

719 Naylor, J., and M. S. Gilmore, 2012: Convective Initiation in an Idealized Cloud Model Using  
720 an Updraft Nudging Technique. *Monthly Weather Review*, **140** (11), 3699–3705, doi:10.1175/  
721 MWR-D-12-00163.1, URL <http://journals.ametsoc.org/doi/abs/10.1175/MWR-D-12-00163.1>.

722 Nolan, D. S., and E. D. Rappin, 2008: Increased sensitivity of tropical cyclogenesis to wind  
723 shear in higher SST environments. *Geophysical Research Letters*, **35** (14), 1–7, doi:10.1029/  
724 2008GL034147.

725 Nowotarski, C. J., P. M. Markowski, Y. P. Richardson, and G. H. Bryan, 2014: Properties of a  
726 Simulated Convective Boundary Layer in an Idealized Supercell Thunderstorm Environment.

727 *Monthly Weather Review*, **142** (11), 3955–3976, doi:10.1175/MWR-D-13-00349.1, URL [http://](http://journals.ametsoc.org/doi/abs/10.1175/MWR-D-13-00349.1)  
728 [journals.ametsoc.org/doi/abs/10.1175/MWR-D-13-00349.1](http://journals.ametsoc.org/doi/abs/10.1175/MWR-D-13-00349.1).

729 Nowotarski, C. J., P. M. Markowski, Y. P. Richardson, and G. H. Bryan, 2015: Supercell Low-  
730 Level Mesocyclones in Simulations with a Sheared Convective Boundary Layer. *Monthly*  
731 *Weather Review*, **143** (1), 272–297, doi:10.1175/MWR-D-14-00151.1, URL [http://journals.](http://journals.ametsoc.org/doi/10.1175/MWR-D-14-00151.1)  
732 [ametsoc.org/doi/10.1175/MWR-D-14-00151.1](http://journals.ametsoc.org/doi/10.1175/MWR-D-14-00151.1).

733 Orf, L., R. Wilhelmson, B. Lee, C. Finley, and A. Houston, 2017: Evolution of a long-track  
734 violent tornado within a simulated supercell. *Bulletin of the American Meteorological Soci-*  
735 *ety*, **98** (1), 45–68, doi:10.1175/BAMS-D-15-00073.1, URL [http://journals.ametsoc.org/doi/10.](http://journals.ametsoc.org/doi/10.1175/BAMS-D-15-00073.1)  
736 [1175/BAMS-D-15-00073.1](http://journals.ametsoc.org/doi/10.1175/BAMS-D-15-00073.1).

737 Parker, M. D., 2014: Composite VORTEX2 Supercell Environments from Near-Storm Soundings.  
738 *Monthly Weather Review*, **142** (2), 508–529, doi:10.1175/MWR-D-13-00167.1, URL [http://](http://journals.ametsoc.org/doi/abs/10.1175/MWR-D-13-00167.1)  
739 [journals.ametsoc.org/doi/abs/10.1175/MWR-D-13-00167.1](http://journals.ametsoc.org/doi/abs/10.1175/MWR-D-13-00167.1).

740 Roberts, B., and M. Xue, 2017: The Role of Surface Drag in Mesocyclone Intensification Lead-  
741 ing to Tornadogenesis within an Idealized Supercell Simulation. *Journal of the Atmospheric*  
742 *Sciences*, **74** (9), 3055–3077, doi:10.1175/JAS-D-16-0364.1, URL [http://journals.ametsoc.org/](http://journals.ametsoc.org/doi/10.1175/JAS-D-16-0364.1)  
743 [doi/10.1175/JAS-D-16-0364.1](http://journals.ametsoc.org/doi/10.1175/JAS-D-16-0364.1).

744 Roberts, B., M. Xue, A. D. Schenkman, and D. T. Dawson, 2016: The Role of Surface Drag  
745 in Tornadogenesis within an Idealized Supercell Simulation. *Journal of the Atmospheric Sci-*  
746 *ences*, **73** (9), 3371–3395, doi:10.1175/JAS-D-15-0332.1, URL [http://journals.ametsoc.org/doi/](http://journals.ametsoc.org/doi/10.1175/JAS-D-15-0332.1)  
747 [10.1175/JAS-D-15-0332.1](http://journals.ametsoc.org/doi/10.1175/JAS-D-15-0332.1).

748 Schenkman, A. D., M. Xue, and D. T. Dawson, 2016: The Cause of Internal Outflow Surges  
749 in a High-Resolution Simulation of the 8 May 2003 Oklahoma City Tornadic Supercell.  
750 *Journal of the Atmospheric Sciences*, **73** (1), 353–370, doi:10.1175/JAS-D-15-0112.1, URL  
751 <http://journals.ametsoc.org/doi/abs/10.1175/JAS-D-15-0112.1>.

752 Schenkman, A. D., M. Xue, and M. Hu, 2014: Tornadogenesis in a High-Resolution Simu-  
753 lation of the 8 May 2003 Oklahoma City Supercell. *Journal of the Atmospheric Sciences*,  
754 **71** (1), 130–154, doi:10.1175/JAS-D-13-073.1, URL <http://journals.ametsoc.org/doi/abs/10.1175/JAS-D-13-073.1>.

756 Skinner, P. S., C. C. Weiss, M. M. French, H. B. Bluestein, P. M. Markowski, and Y. P. Richardson,  
757 2014: VORTEX2 Observations of a Low-Level Mesocyclone with Multiple Internal Rear-Flank  
758 Downdraft Momentum Surges in the 18 May 2010 Dumas, Texas, Supercell\*. *Monthly Weather*  
759 *Review*, **142** (8), 2935–2960, doi:10.1175/MWR-D-13-00240.1, URL <http://journals.ametsoc.org/doi/abs/10.1175/MWR-D-13-00240.1>.

761 Skinner, P. S., C. C. Weiss, J. L. Schroeder, L. J. Wicker, and M. I. Biggerstaff, 2011: Observations  
762 of the Surface Boundary Structure within the 23 May 2007 Perryton, Texas, Supercell. *Monthly*  
763 *Weather Review*, (June 1995), 3730–3749, doi:10.1175/MWR-D-10-05078.1.

764 Wicker, L. J., and R. B. Wilhelmson, 1993: Numerical Simulation of Tornadogenesis Within  
765 a Supercell Thunderstorm. *The Tornado: Its Structure, Dynamics, Prediction, and Hazards*,  
766 American Geophysical Union, 75–88.

767 Wilhelmson, R. B., and C.-S. Chen, 1982: A Simulation of the Development of Suc-  
768 cessive Cells Along a Cold Outflow Boundary. *Journal of the Atmospheric Sciences*,  
769 **39** (7), 1466–1483, doi:10.1175/1520-0469(1982)039<1466:ASOTDO>2.0.CO;2, URL

770 [http://journals.ametsoc.org/doi/abs/10.1175/1520-0469{\\%}281982{\\%}29039{\\%](http://journals.ametsoc.org/doi/abs/10.1175/1520-0469{\\%}281982{\\%}29039{\\%})  
771 [}3C1466{\\%}3AASOTDO{\\%}3E2.0.CO{\\%}3B2.](http://journals.ametsoc.org/doi/abs/10.1175/1520-0469{\\%}281982{\\%}29039{\\%}3C1466{\\%}3AASOTDO{\\%}3E2.0.CO{\\%}3B2)

772 **LIST OF TABLES**

773 **Table 1.** Simulation configuration . . . . . 37

TABLE 1. Simulation configuration

<b>Experiment naming key:</b> S=storm, NS=no storm, T=resolved BL turbulence, NT=no resolved BL turbulence, D=surface drag, ND=no surface drag	
<b>Experiment Names</b>	<b>Description</b>
[S, NS]-[T, NT]-ND-GEO	No surface drag with initial geostrophic balance
[S, NS]-[T, NT]-ND-GWB	No surface drag with GWB method applied
[S, NS]-[T, NT]-D-GEO	With surface drag and initial geostrophic balance
[S, NS]-[T, NT]-D-GWB	With surface drag with GWB method applied
[S, NS]-[T, NT]-D-WC	With surface drag but with base-state surface drag removed (Wilhelmson and Chen 1982)

774 **LIST OF FIGURES**

775 **Fig. 1.** Skew-T and Hodograph for the RUC-derived 24 May 2011 inflow sounding used in the  
776 simulation experiments. . . . . 39

777 **Fig. 2.** Hodographs for each of the no-storm runs without resolved boundary layer turbulence (NS-  
778 NT-). For clarity, only the lower portions of the hodographs are plotted. The hodographs  
779 were computed from a weighted (by grid-cell area) horizontal average of the entire domain.  
780 Initial hodographs are shown in black, while the 1-, 2-, and 3-h forecast times are shown  
781 in blue with changing line styles (see legend). Red markers (see legend) indicate specific  
782 heights (m AGL). time. . . . . 40

783 **Fig. 3.** Timeseries of domain maximum (a) vertical velocity ( $\text{m s}^{-1}$ ), (b) surface vertical vorticity  
784 ( $\text{s}^{-1}$ ), and (c) surface wind speed ( $\text{m s}^{-1}$ ) for each of the storm simulations without resolved  
785 boundary layer turbulence (the S-NT- simulations). The black vertical lines denote the start  
786 and end times of the temporal composites described in section 4 . . . . . 41

787 **Fig. 4.** As in Fig. 2 but for the storm simulations without resolved boundary layer turbulence (S-  
788 NT-). . . . . 42

789 **Fig. 5.** As in Fig. 3a but for the no-storm simulations with resolved boundary layer turbulence  
790 (NS-T-). . . . . 43

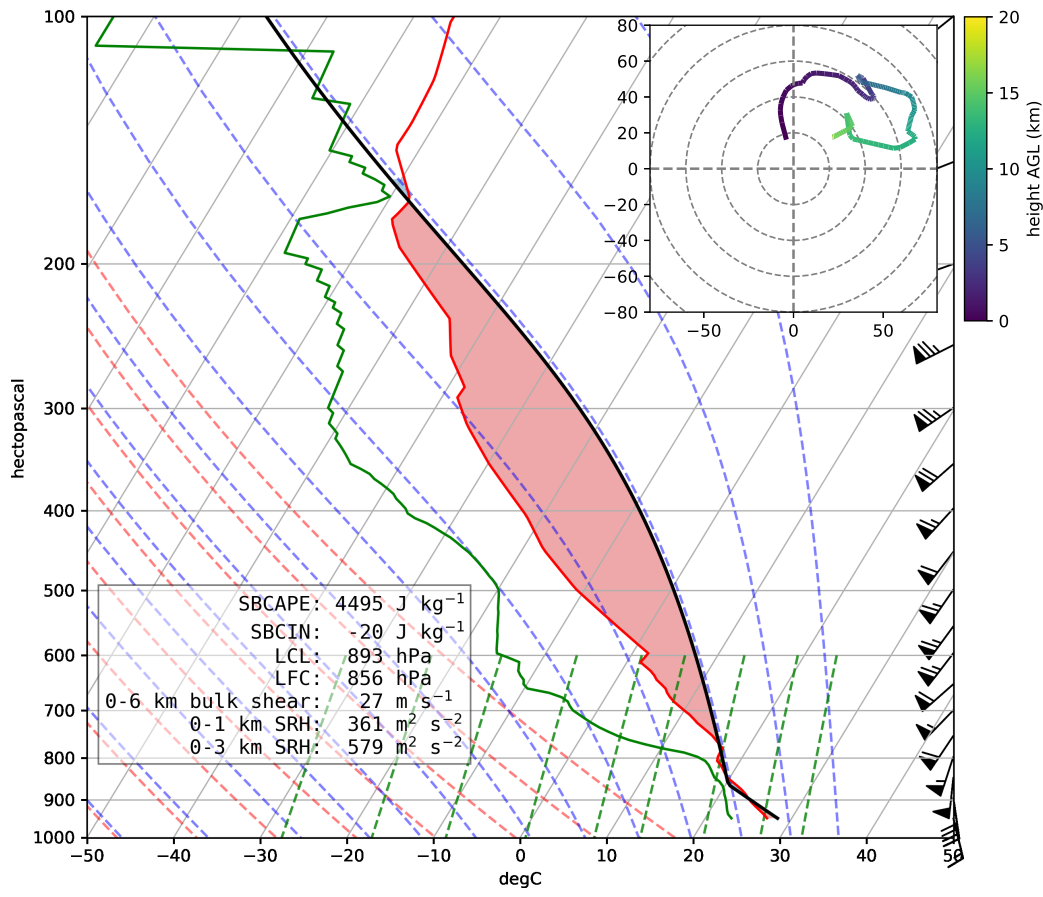
791 **Fig. 6.** Vertical profiles valid at 2 h of inner domain horizontal mean subgrid-scale (solid), resolved  
792 (dashed), and total (dotted) TKE for each of the NS-NT- (left column) and NS-T- (right  
793 column) simulations. Red markers indicate the same heights AGL as in Figs. 2 and 4. . . . . 44

794 **Fig. 7.** As in Fig. 2 but for the no-storm simulations with turbulent boundary layer (NS-T-) runs. . . . . 45

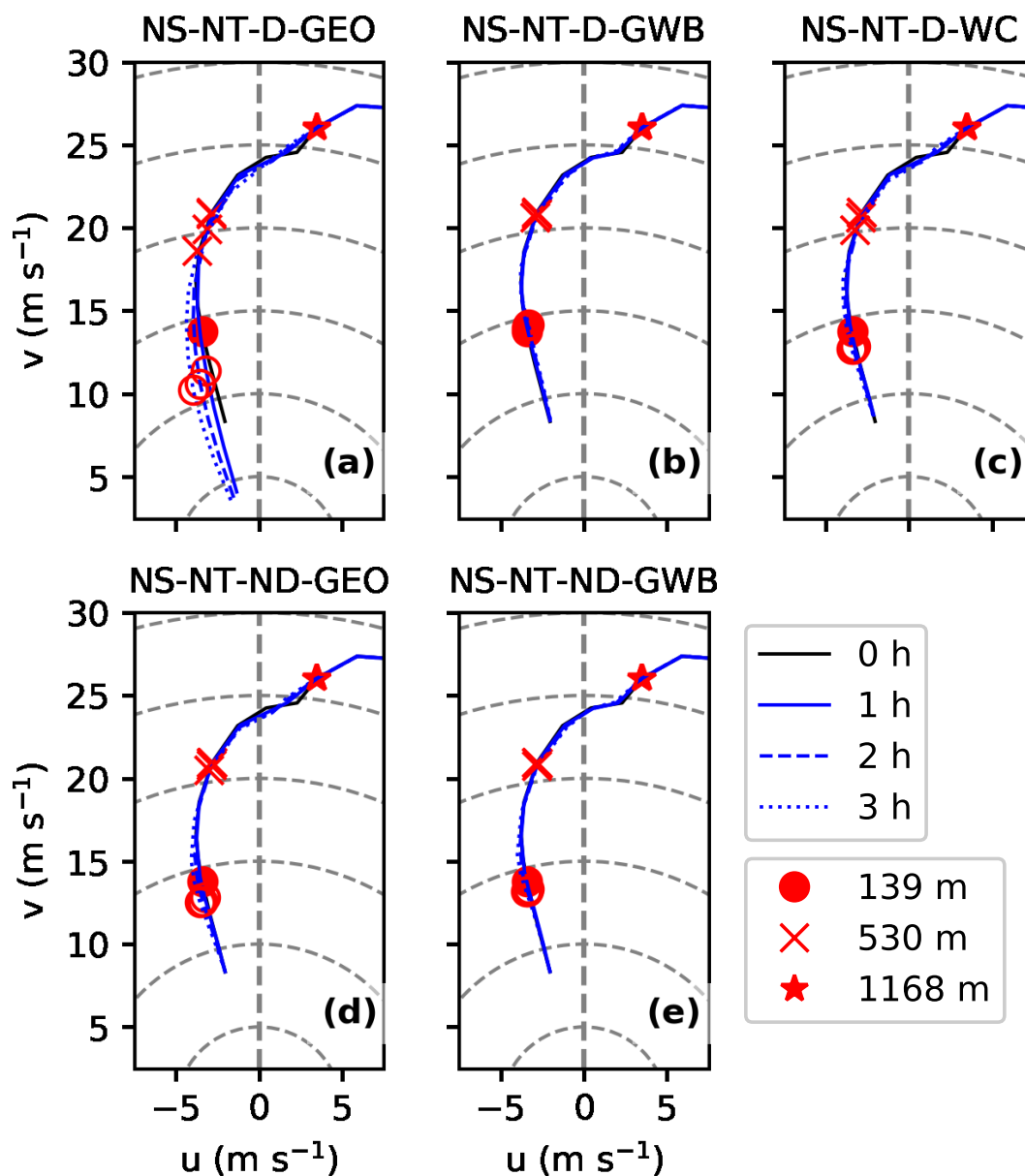
795 **Fig. 8.** Vertical profiles of the meridional component of (a) the PPGF acceleration and (b) the fric-  
796 tional force for the four no-storm GWB experiments. Red and blue curves indicate the  
797 experiments with and without surface drag, respectively. Solid and dashed curves are for the  
798 experiments without and with resolved BL turbulence, respectively. For the resolved-BL-  
799 turbulence experiments, the PPGF profile is shown for a model time of 2 h. The profile of  
800 the average Coriolis force (which is nearly identical between the four experiments since it  
801 depends only on the nearly constant vertical wind profile) is also shown for (black dotted  
802 line) for reference in panel (a). Note the symmetric logarithmic scale for the abscissa. . . . . 46

803 **Fig. 9.** As in Fig. 7 but for the storm simulations with turbulent boundary layer (S-T-) runs. . . . . 47

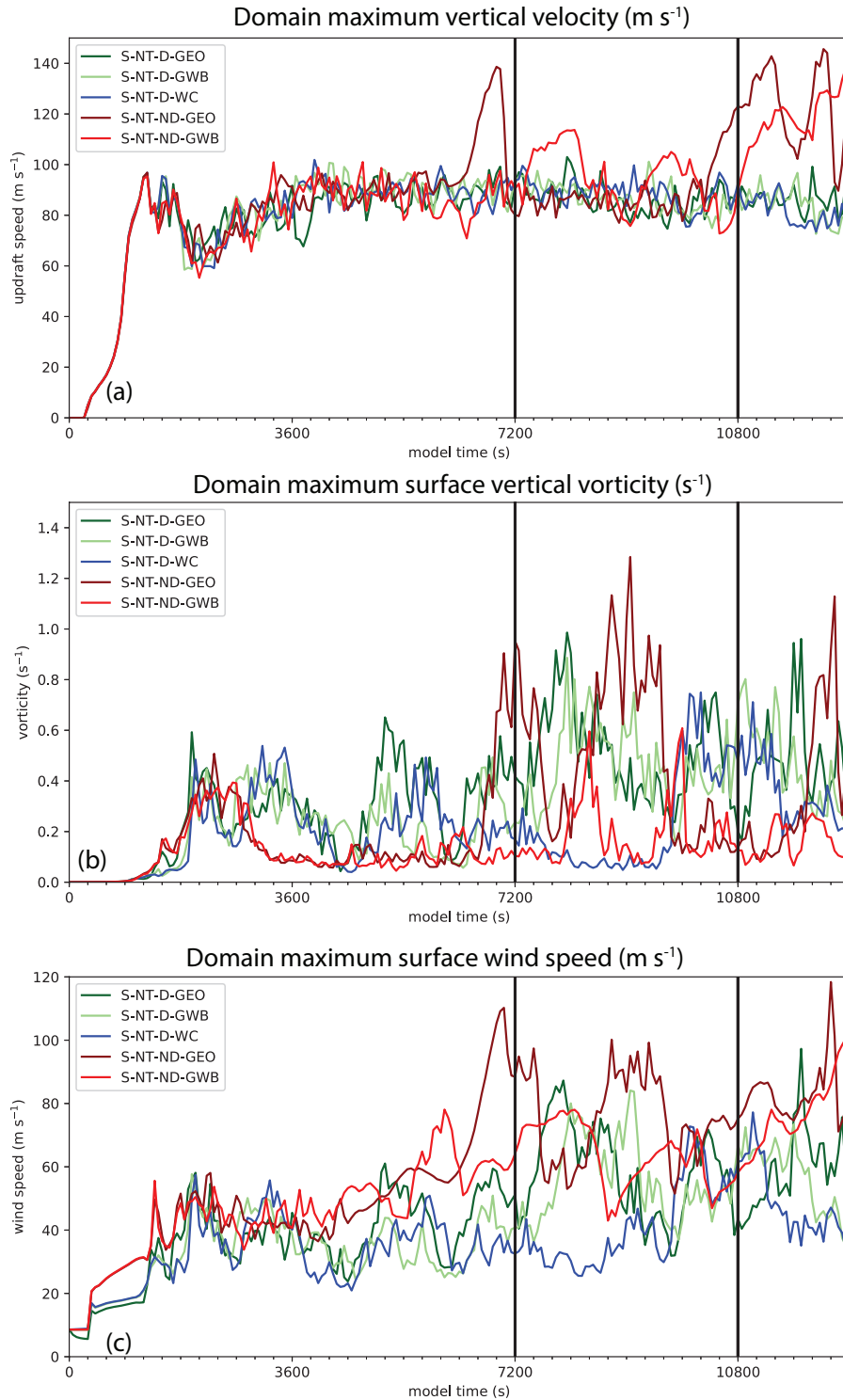
804 **Fig. 10.** Temporal composites (see text for details on the construction of the composites) centered  
805 on the location of maximum surface vorticity for each of the S-NT- runs. Shown in each  
806 composite is ground-relative surface wind speed (HWS; color fill,  $\text{m s}^{-1}$ ), surface asymp-  
807 totic contraction rate (ACR; green contour;  $0.0075 \text{ s}^{-1}$  shown), and radar reflectivity (black  
808 contours, 10 dBZ increment, starting at 20 dBZ). . . . . 48



809 FIG. 1. Skew-T and Hodograph for the RUC-derived 24 May 2011 inflow sounding used in the simulation  
 810 experiments.



811 FIG. 2. Hodographs for each of the no-storm runs without resolved boundary layer turbulence (NS-NT-). For  
 812 clarity, only the lower portions of the hodographs are plotted. The hodographs were computed from a weighted  
 813 (by grid-cell area) horizontal average of the entire domain. Initial hodographs are shown in black, while the 1-,  
 814 2-, and 3-h forecast times are shown in blue with changing line styles (see legend). Red markers (see legend)  
 815 indicate specific heights (m AGL). time.



816 FIG. 3. Timeseries of domain maximum (a) vertical velocity ( $\text{m s}^{-1}$ ), (b) surface vertical vorticity ( $\text{s}^{-1}$ ), and  
 817 (c) surface wind speed ( $\text{m s}^{-1}$ ) for each of the storm simulations without resolved boundary layer turbulence (the  
 818 S-NT- simulations). The black vertical lines denote the start and end times of the temporal composites described  
 819 in section 4

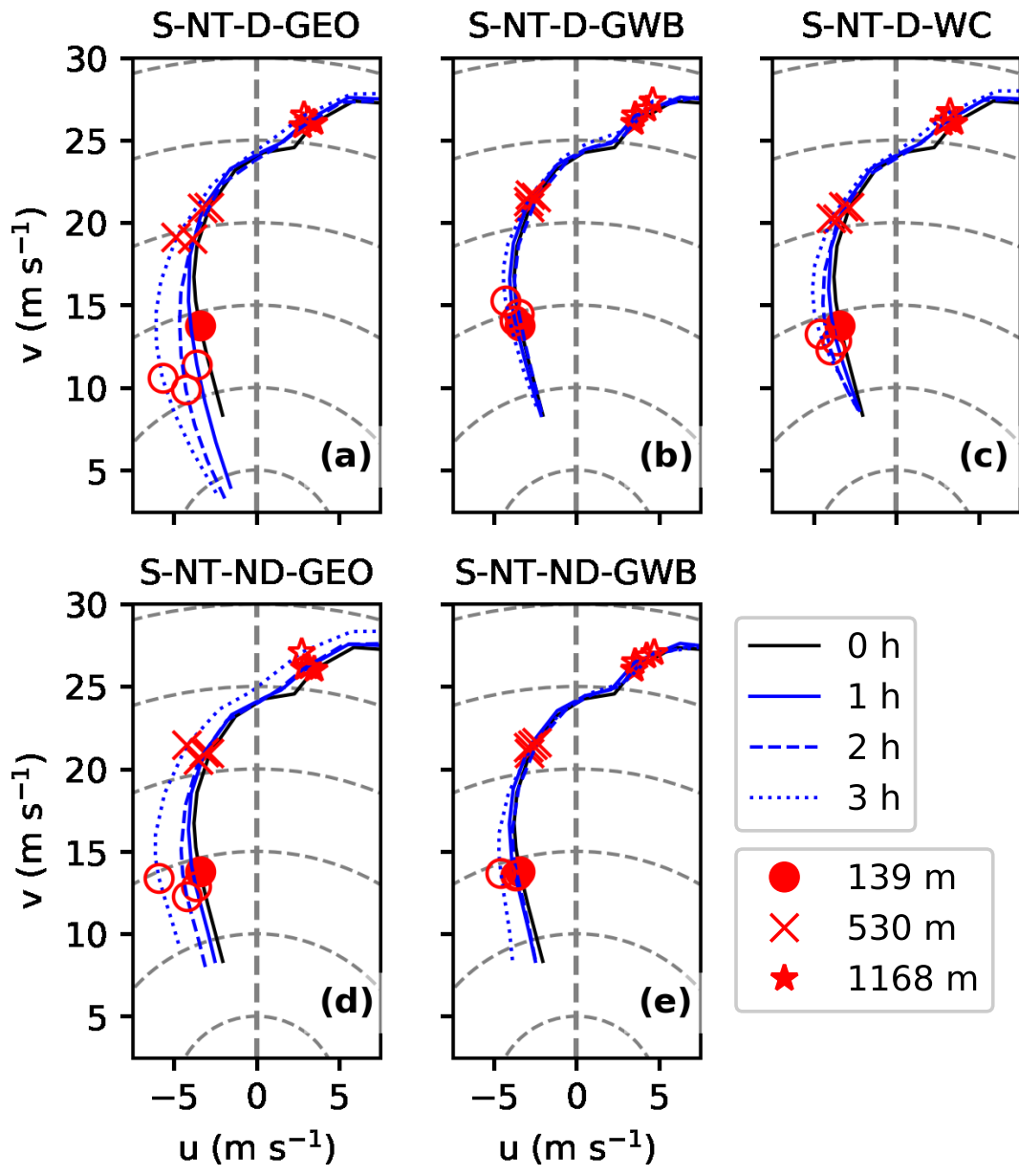


FIG. 4. As in Fig. 2 but for the storm simulations without resolved boundary layer turbulence (S-NT-).

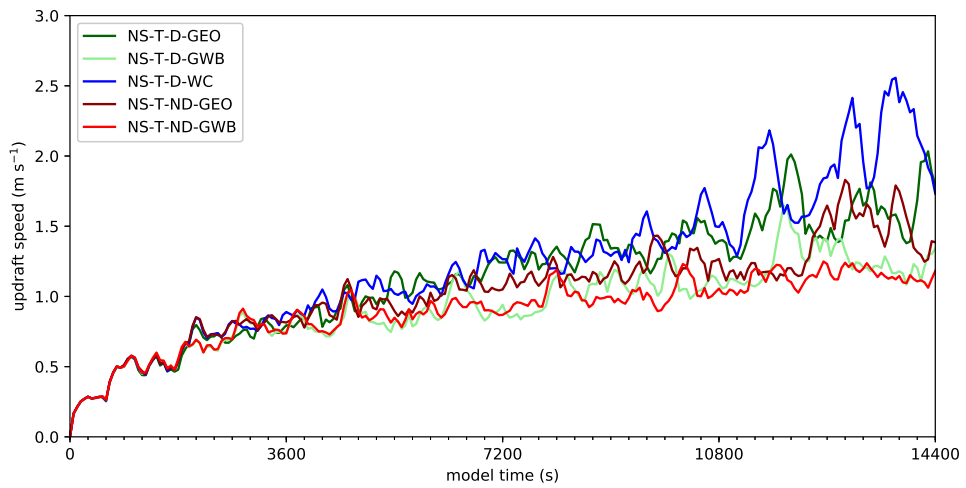
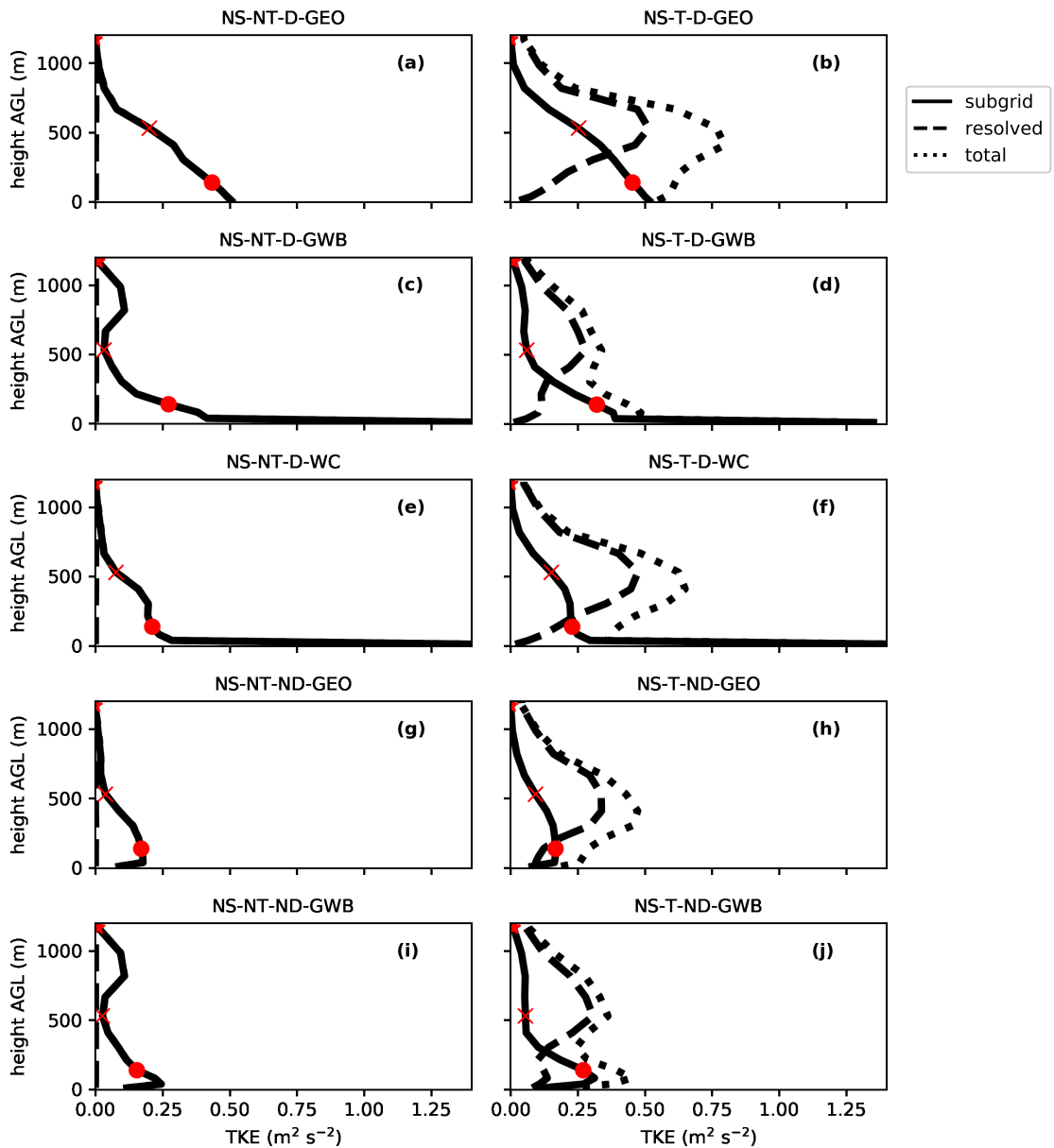


FIG. 5. As in Fig. 3a but for the no-storm simulations with resolved boundary layer turbulence (NS-T).



820 FIG. 6. Vertical profiles valid at 2 h of inner domain horizontal mean subgrid-scale (solid), resolved (dashed),  
 821 and total (dotted) TKE for each of the NS-NT- (left column) and NS-T- (right column) simulations. Red markers  
 822 indicate the same heights AGL as in Figs. 2 and 4.

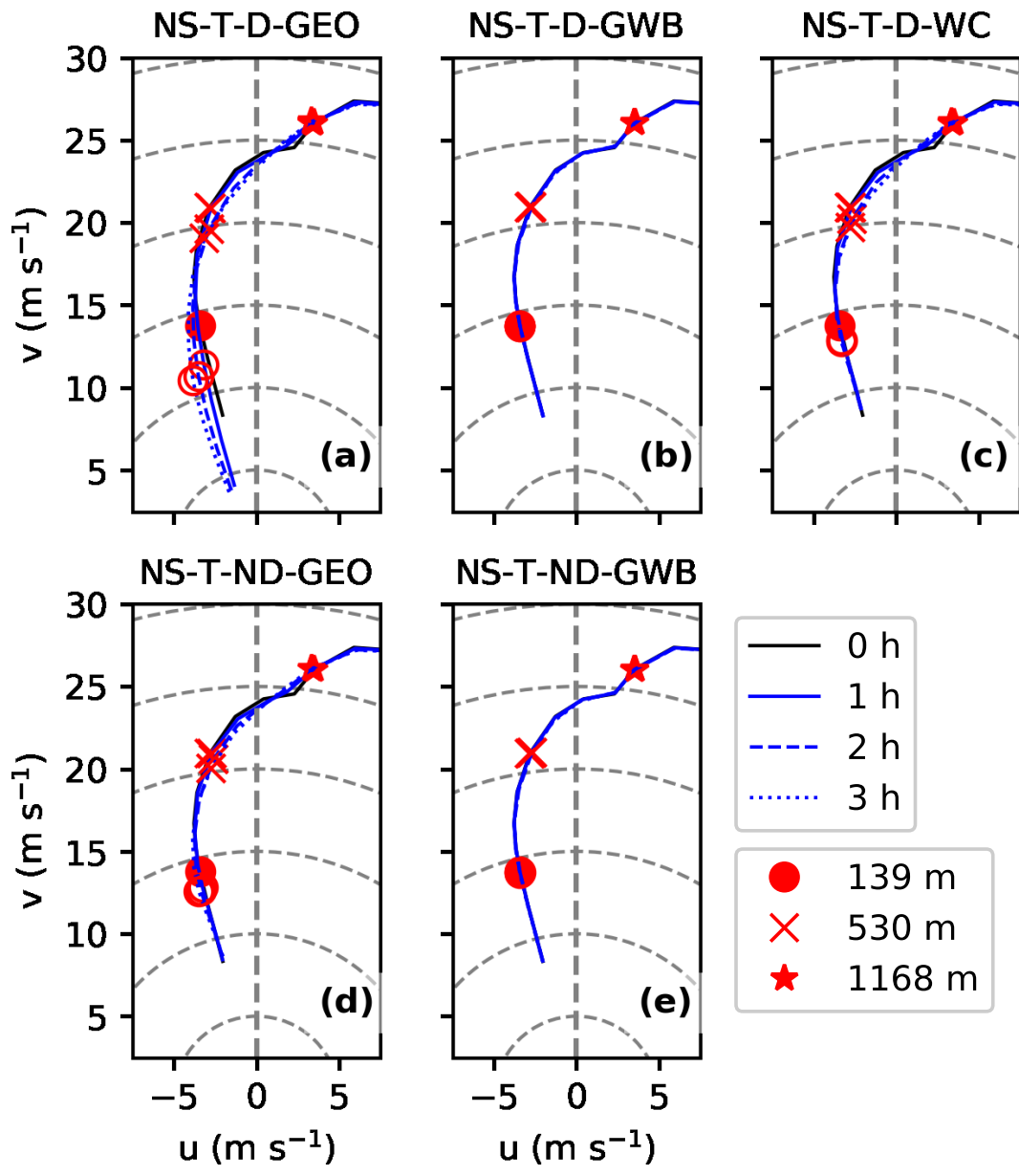
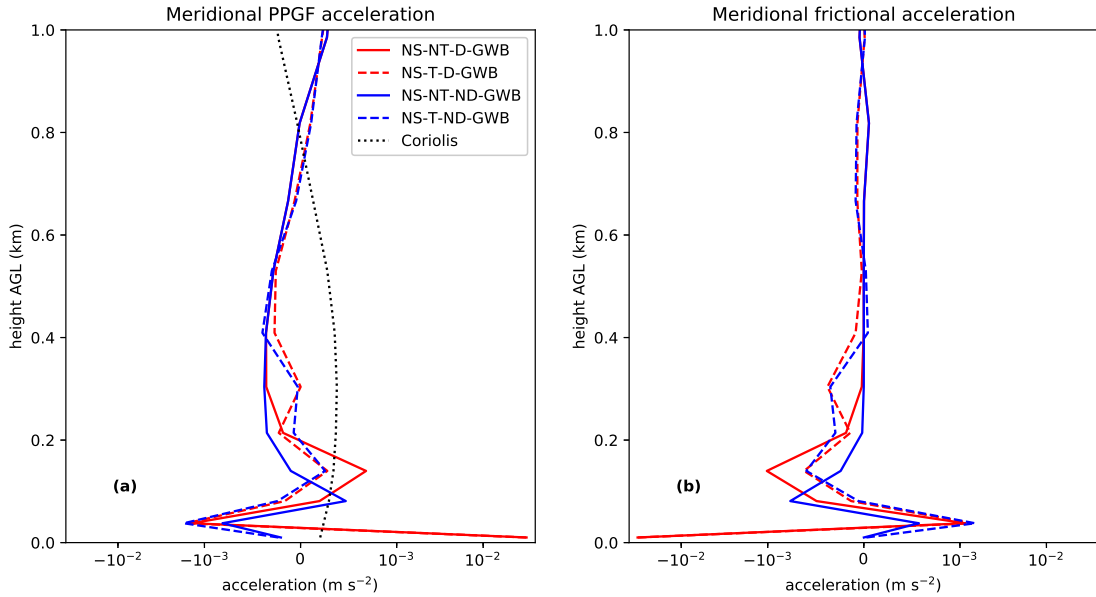


FIG. 7. As in Fig. 2 but for the no-storm simulations with turbulent boundary layer (NS-T-) runs.



823 FIG. 8. Vertical profiles of the meridional component of (a) the PPGF acceleration and (b) the frictional force  
 824 for the four no-storm GWB experiments. Red and blue curves indicate the experiments with and without surface  
 825 drag, respectively. Solid and dashed curves are for the experiments without and with resolved BL turbulence,  
 826 respectively. For the resolved-BL-turbulence experiments, the PPGF profile is shown for a model time of 2 h.  
 827 The profile of the average Coriolis force (which is nearly identical between the four experiments since it depends  
 828 only on the nearly constant vertical wind profile) is also shown for (black dotted line) for reference in panel  
 829 (a). Note the symmetric logarithmic scale for the abscissa.

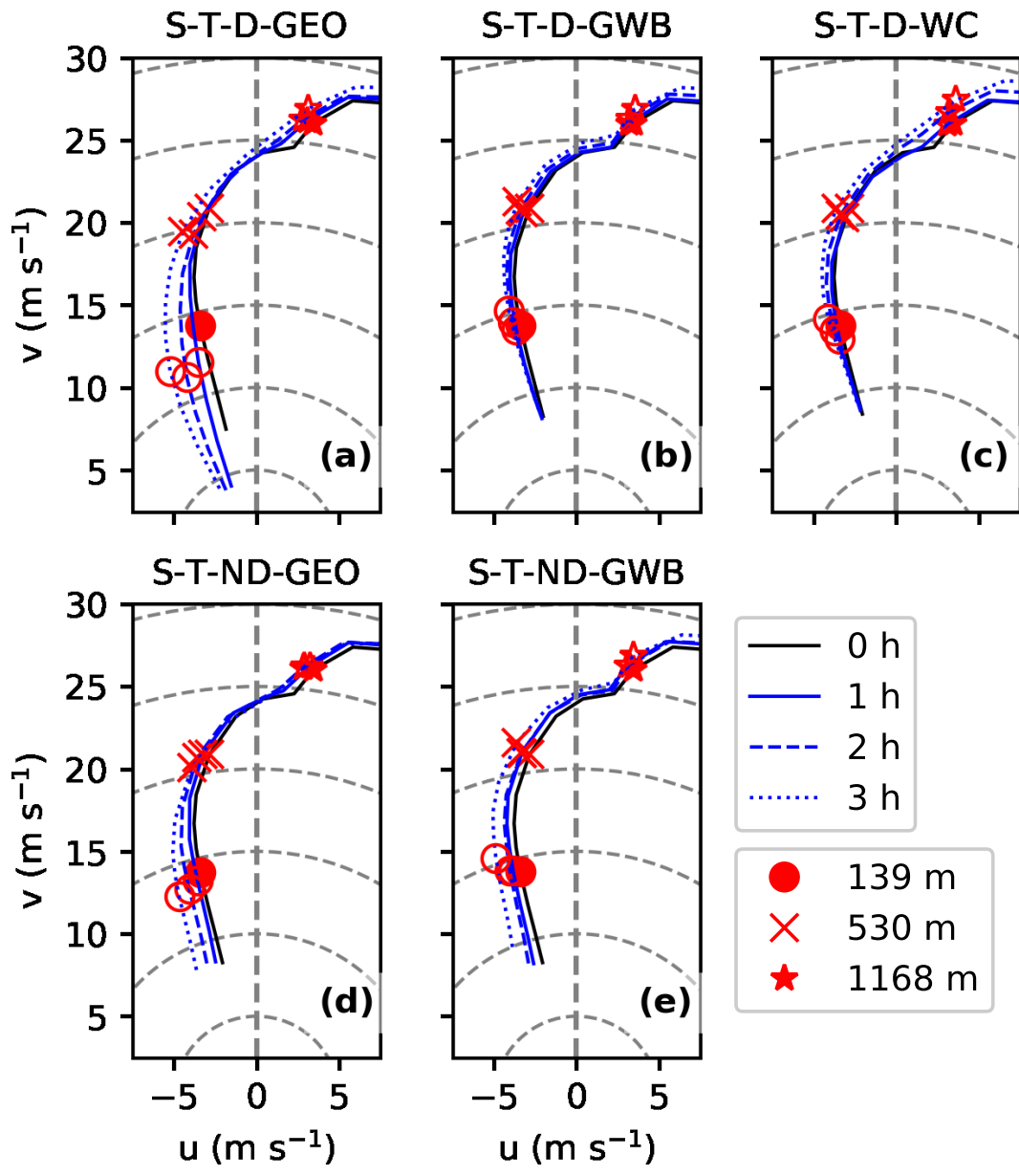
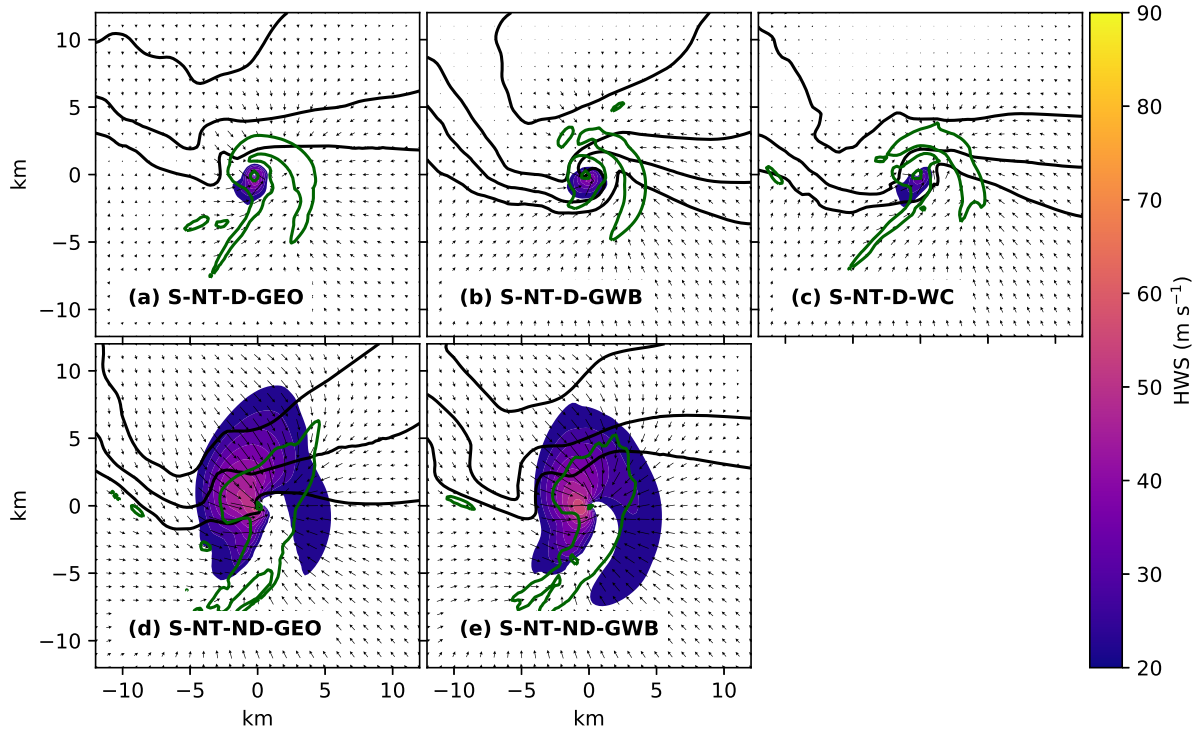


FIG. 9. As in Fig. 7 but for the storm simulations with turbulent boundary layer (S-T-) runs.



830 FIG. 10. Temporal composites (see text for details on the construction of the composites) centered on the  
 831 location of maximum surface vorticity for each of the S-NT- runs. Shown in each composite is ground-relative  
 832 surface wind speed (HWS; color fill,  $\text{m s}^{-1}$ ), surface asymptotic contraction rate (ACR; green contour;  $0.0075$   
 833  $\text{s}^{-1}$  shown), and radar reflectivity (black contours, 10 dBZ increment, starting at 20 dBZ).